Published in final edited form as:
Med (N Y). 2021 January 15; 2(1): 49–73. doi:10.1016/j.medj.2020.06.004.

Fatal perinatal mitochondrial cardiac failure caused by recurrent *de novo* duplications in the *ATAD3* locus

Ann E. Frazier[1,2,31], **Alison G. Compton**[1,2,31], **Yoshihito Kishita**[3], **Daniella H. Hock**[4], **AnneMarie E. Welch**[1], **Sumudu S.C. Amarasekera**[1,2], **Rocio Rius**[1,2], **Luke E. Formosa**[5], **Atsuko Imai-Okazaki**[3,6], **David Francis**[7], **Min Wang**[1], **Nicole J. Lake**[1,2,8], **Simone Tregoning**[1,7], **Jafar S. Jabbari**[9], **Alexis Lucattini**[9], **Kazuhiro R. Nitta**[3], **Akira Ohtake**[10], **Kei Murayama**[11], **David J. Amor**[1,2], **George McGillivray**[7], **Flora Y. Wong**[12], **Marjo S. van der Knaap**[13,14], **R. Jeroen Vermeulen**[15], **Esko J. Wiltshire**[16], **Janice M. Fletcher**[17], **Barry Lewis**[18], **Gareth Baynam**[19,20], **Carolyn Ellaway**[21,22], **Shanti Balasubramaniam**[21], **Kaustuv Bhattacharya**[21,22], **Mary-Louise Freckmann**[23], **Susan Arbuckle**[24], **Michael Rodriguez**[25], **Ryan J. Taft**[26], **Simon Sadedin**[1,7], **Mark J. Cowley**[27,28], **André E. Minoche**[28], **Sarah E. Calvo**[29], **Vamsi K. Mootha**[29], **Michael T. Ryan**[5], **Yasushi Okazaki**[3], **David A. Stroud**[4], **Cas Simons**[1,30,*], **John Christodoulou**[1,2,7,22,*], **David R. Thorburn**[1,2,7,32,*]

[1]Murdoch Children's Research Institute, Royal Children's Hospital, Melbourne, VIC 3052, Australia [2]Department of Paediatrics, University of Melbourne, Melbourne, VIC 3052, Australia [3]Diagnostics and Therapeutics of Intractable Diseases, Intractable Disease Research Center, Juntendo University, Graduate School of Medicine, Tokyo, 113-8421, Japan [4]Department of Biochemistry and Molecular Biology and Bio21 Molecular Science and Biotechnology Institute, University of Melbourne, Melbourne, VIC 3052, Australia [5]Department of Biochemistry and Molecular Biology, Monash Biomedicine Discovery Institute, Monash University, Melbourne, VIC 3800, Australia [6]Division of Genomic Medicine Research, Medical Genomics Center, National Center for Global Health and Medicine, Tokyo 162-8655, Japan [7]Victorian Clinical Genetics Services, Murdoch Children's Research Institute, Royal Children's Hospital, Melbourne, VIC 3052, Australia [8]Department of Genetics, Yale School of Medicine, New Haven, CT 06510, USA [9]Australian Genome Research Facility Ltd, Victorian Comprehensive Cancer Centre, Melbourne VIC 3052, Australia [10]Department of Pediatrics & Clinical Genomics, Saitama Medical University Hospital, Saitama, 350-0495, Japan [11]Department of Metabolism, Chiba Children's Hospital, Chiba, 266-0007, Japan [12]Ritchie Centre, Hudson Institute of Medical Research; Department of

---

[*] Correspondance: David R. Thorburn: david.thorburn@mcri.edu.au, John Christodoulou: john.christodoulou@mcri.edu.au, Cas Simons: cas.simons@mcri.edu.au.

Author Contributions
AEF, AGC, CS, DRT, JC conceived the study.
AEW, AEF, YK, AGC, RR, DHH, DAS, SSCA, SEC, NJL, LEF, DF acquired the data.
AEF, AGC, YK, DHH, DAS, RR, LEF, DRT, CS, DF, MTR, YO analyzed and interpreted the data.
AEF, AEW, AGC, YK, NJL, RR, CS, RJT, AEM, JSJ, AL, KRN, MW, SS, MJC, SEC, VKM, DHH, DAS performed the bioinformatic, genomic or proteomic analyses.
AIO, AO, KM, MSK, RJV, GB, JC, DJA, GM, FYW, EJW, JMF, BL, CE, SB, KB, MLF, SA, MR, ST, DRT recruited patients, liaised with families and collected and reviewed clinical and diagnostic data
AEF, AGC, DRT, DAS wrote the manuscript, with input from all authors.
All authors reviewed and approved the manuscript.

Declaration of Interests
RJT is an employee of Illumina, Inc.

Paediatrics, Monash University; and Monash Newborn, Monash Children's Hospital, Melbourne, VIC 3168, Australia. [13]Child Neurology, Emma Children's Hospital, Amsterdam University Medical Centers, Vrije Universiteit and Amsterdam Neuroscience, 1081 HV Amsterdam, The Netherlands [14]Functional Genomics, Center for Neurogenomics and Cognitive Research, Vrije Universiteit and Amsterdam Neuroscience, 1081 HV Amsterdam, The Netherlands [15]Department of Neurology, Maastricht University Medical Center, 6229 HX, Maastricht, The Netherlands [16]Department of Paediatrics and Child Health, University of Otago Wellington and Capital and Coast District Health Board, Wellington 6021, New Zealand [17]Department of Genetics and Molecular Pathology, SA Pathology, Adelaide, SA 5000, Australia [18]Department of Clinical Biochemistry, PathWest Laboratory Medicine Western Australia, Nedlands, WA 6009, Australia [19]Western Australian Register of Developmental Anomalies and Genetic Services of Western Australia and King Edward Memorial Hospital for Women Perth, Subiaco, WA 6008, Australia [20]Telethon Kids Institute and School of Paediatrics and Child Health, The University of Western Australia, Perth, WA 6009, Australia [21]Genetic Metabolic Disorders Service, Sydney Children's Hospital Network, The Children's Hospital at Westmead, Sydney, NSW 2145, Australia [22]Disciplines of Genomic Medicine and Child and Adolescent Health, Sydney Medical School, University of Sydney, NSW 2145, Australia [23]Clinical Genetics, The Canberra Hospital, Garran, ACT 2605, Australia [24]Department of Histopathology, The Children's Hospital at Westmead, Sydney Children's Hospital Network, Sydney, NSW 2145, Australia [25]Discipline of Pathology, School of Medical Sciences, The University of Sydney, Sydney, NSW 2006, Australia [26]Illumina, Inc., San Diego, CA 92121, USA [27]Children's Cancer Institute, Kensington, NSW 2750, Australia; St Vincent's Clinical School, UNSW Sydney, Darlinghurst, NSW 2010, Australia [28]Kinghorn Centre for Clinical Genomics, Garvan Institute of Medical Research, Darlinghurst, NSW 2010, Australia [29]Broad Institute, Cambridge, MA 02142, USA; Howard Hughes Medical Institute and Department of Molecular Biology, Massachusetts General Hospital, Boston, MA 02114, USA; Harvard Medical School, Boston, MA 02446, USA [30]Institute for Molecular Bioscience, The University of Queensland, Brisbane, QLD 4072 Australia [31]These authors contributed equally: A.E. Frazier, A.G. Compton [32]Lead contact

Abstract

Background—In about half of all patients with a suspected monogenic disease, genomic investigations fail to identify the diagnosis. A contributing factor is the difficulty with repetitive regions of the genome, such as those generated by segmental duplications. The *ATAD3* locus is one such region, in which recessive deletions and dominant duplications have recently been reported to cause lethal perinatal mitochondrial diseases characterized by pontocerebellar hypoplasia or cardiomyopathy, respectively.

Methods—Whole exome, whole genome and long-read DNA sequencing techniques combined with studies of RNA and quantitative proteomics were used to investigate 17 subjects from 16 unrelated families with suspected mitochondrial disease.

Findings—We report six different *de novo* duplications in the *ATAD3* gene locus causing a distinctive presentation including lethal perinatal cardiomyopathy, persistent hyperlactacidemia, and frequently corneal clouding or cataracts and encephalopathy. The recurrent 68 Kb *ATAD3* duplications are identifiable from genome and exome sequencing but usually missed by microarrays. The *ATAD3* duplications result in the formation of identical chimeric ATAD3A/ATAD3C proteins, altered ATAD3 complexes and a striking reduction in mitochondrial oxidative phosphorylation complex I and its activity in heart tissue.

Conclusions—*ATAD3* duplications appear to act in a dominant-negative manner and the *de novo* inheritance infers a low recurrence risk for families, unlike most pediatric mitochondrial diseases. More than 350 genes underlie mitochondrial diseases. In our experience the *ATAD3* locus is now one of the five most common causes of nuclear-encoded pediatric mitochondrial disease but the repetitive nature of the locus means *ATAD3* diagnoses may be frequently missed by current genomic strategies.

Funding—Australian NHMRC, US Department of Defense, Japanese AMED and JSPS agencies, Australian Genomics Health Alliance and Australian Mito Foundation.

Keywords

cardiomyopathy; ATAD3; segmental duplication; mitochondrial disease; genomics; quantitative proteomics

Introduction

Mitochondrial energy generation diseases are the most common group of inherited metabolic diseases, affecting at least 20 per 100,000 births[1], but comprise more than 350 monogenic disorders[2]. Most childhood-onset mitochondrial diseases are thought to have autosomal recessive inheritance, with mitochondrial DNA (mtDNA) mutations responsible for about a quarter of cases and other inheritance mechanisms apparently less common[1]. However, as with many other genetic disorders, up to half of all patients with suspected disease remain without a molecular diagnosis after genomic investigations[3]. This is partly due to technical limitations and the clinical challenges of interpretation, but another contributor is the genomic architecture of repetitive regions of the genome.

Segmental duplications, also known as low-copy repeats, are highly homologous duplicated sequences that exist in one or more copies within a genome[4,5]. The human genome is estimated to consist of ~50% repeat sequences with segmental duplications thought to account for ~5% of these[5–7]. Intrachromosomal segmental duplications can make regions structurally unstable and prone to DNA rearrangements via nonallelic homologous recombination (NAHR)[8]. These rearrangements can result in structural or copy number variation (CNV), such as duplications and deletions, and have been demonstrated to underlie numerous syndromes[8,9] with over 40 “genomic disorders” identified[8,10].

Perhaps the most complex genomic site linked to mitochondrial disease, the *ATAD3* segmental duplication contains three highly homologous tandemly arrayed genes: *ATAD3C*, *ATAD3B*, and *ATAD3A*. This arrangement is exclusive to hominids, with a single copy of *ATAD3* found in other multicellular organisms[11]. In mice, *D. melanogaster* and *C. elegans,* loss of ATAD3 (ATPase family AAA+ domain-containing member 3) causes early embryonic or larval lethality[12–14]. In 2016, pathogenic variants in *ATAD3* were linked to Harel-Yoon Syndrome (HAYOS; MIM: 617183), characterized by global developmental delay and hypotonia, along with other features including axonal neuropathy, optic atrophy or cataracts, cerebellar atrophy and hypertrophic cardiomyopathy[15]. A variety of genetic mechanisms have now been reported in this locus including *de novo* dominant single nucleotide variants (SNVs)[15], inherited dominant SNVs[16], inherited recessive SNVs[15,17,18], and *ATAD3* gene conversions[19]. More severe presentations characterized by fatal congenital pontocerebellar hypoplasia and sometimes cardiomyopathy, often with cataracts or corneal clouding, have been linked to *ATAD3* variation in multiple patients, the majority with inherited recessive deletions affecting *ATAD3A* and *ATAD3B* (MIM: 618810)[15,17,19]. Likewise, dominant *de novo* duplications involving *ATAD3C*, *ATAD3B* and *ATAD3A* have recently been reported in five patients with fatal cardiomyopathy and corneal clouding/cataracts (MIM: 618815)[20]. These *ATAD3* CNVs are thought to arise via NAHR-mediated events within the repetitive *ATAD3* locus[15], resulting in chimeric *ATAD3* genes[15,19,20] (Figure 1A).

ATAD3 localizes to the mitochondrial inner membrane with its N-terminus in the intermembrane space, potentially contacting the mitochondrial outer membrane [12,21]. It is found predominantly at the boundary between the inner and outer membranes, rather than in the cristae[22], with enrichment also at mitochondria/endoplasmic reticulum contact sites in humans and mice[23–25]. The precise molecular functions of ATAD3 are unresolved and it has been linked to diverse mitochondrial roles[21]. Two major roles appear to be in (i) hormone induced steroidogenesis[12,23], possibly via organization of cholesterol transfer between the endoplasmic reticulum and mitochondria[12,26,27]; and (ii) mtDNA organization and segregation, as ATAD3 can be purified as an mtDNA nucleoid component[28] and can influence the co-fractionation of mtDNA and cholesterol[22]. Other functions ascribed to ATAD3 include roles in mitochondrial translation[27], adipogenesis and lipid metabolism[13,29], iron and heme homeostasis[30] and maintenance of mitochondrial networks[12,16,31,32], with ATAD3 reported to interact with mitochondrial fission mediator DRP1[33]. Expression of mutant ATAD3 is reported to increase autophagy and mitophagy[15,16], with ATAD3 proposed to suppress mitophagy by mediating mitochondrial import and degradation of PINK1 in mice[34].

Here, we show that the *ATAD3* locus is a hotspot for pathogenic genomic variation leading to mitochondrial disease by describing 17 patients from 16 families with recurrent 68 Kb duplications in the *ATAD3* locus (*ATAD3*dup). These duplications generate an extra copy of the *ATAD3B* gene and an in-frame *ATAD3A/ATAD3C* fusion gene that generates a stable chimeric ATAD3A/ATAD3C protein that disrupts ATAD3 oligomerization.

Results

Identification of recurrent de novo ATAD3 duplications

A heterozygous *de novo* duplication within the *ATAD3* locus (GRCh37/hg19; chr1:g.1,385,069 – 1,470,067) was initially identified in a patient (P1) from trio whole genome sequencing (WGS) (Figure 1B). Similar to previously reported patients with biallelic *ATAD3* deletions (*ATAD3*del)[15,17,19], her clinical phenotype included hyperlactacidemia, cataracts, white matter abnormalities and perinatal death (Table 1 and individual case reports in Table S1). Strikingly, hypertrophic cardiomyopathy was also observed in this patient, but not commonly noted in *ATAD3*del patients[15,17,19]. Likewise, compared to the severe pontocerebellar hypoplasia characteristically observed in *ATAD3*del patients, P1 had only mild pontocerebellar defects.

Re-inspection of available data from WGS and/or whole exome sequencing (WES) of unsolved patients with suspected perinatal or infantile lethal mitochondrial disease revealed 13 additional patients (P2a & b – P13, including monozygotic twins) from 12 families with remarkably similar *ATAD3* duplications, detected using a variety of CNV callers including CNVnator[35], ExomeDepth[36], and XHMM[37] (Figures 1B, 1C, S1A, S1B; See methods for individual details). The duplications detected by WES were supported by read depth data from linked-read Chromium WGS (10x Genomics) across the *ATAD3* locus for four of the patients (Figure 1B).

An additional *ATAD3*dup patient (P15) was identified from an in-house clinical SNP microarray database (VCGS; consisting of ~90,000 previously tested patients). The microarray was performed as part of prenatal testing (post-amniocentesis) after an ultrasound scan at 31 weeks gestation indicated the presence of cardiac hypertrophy (Figure S1C). Parental microarray screening indicated the *ATAD3* CNV was *de novo*. We note that microarrays can show poor sensitivity for CNV detection within segmental duplications[38] and the probe coverage across the *ATAD3* locus is limited on many array platforms, making identification of *ATAD3* CNVs challenging[15,39]. The *ATAD3* duplication was only detected in only one of five other confirmed *ATAD3*dup patients screened on the same array platform (Figure S1C). Therefore, it was not surprising that no other samples with similar *ATAD3* duplications were identified within our clinical database.

Duplication CNVs most commonly occur in tandem[40], so using the *ATAD3A*/*ATAD3C* breakpoints predicted from the sequencing and array technologies, genomic DNA PCR screens were developed to confirm the CNV structure and evaluate inheritance. In all patients, a PCR product spanning the *ATAD3A*/*ATAD3C* breakpoint was amplified that enabled molecular determination of the *ATAD3* duplication breakpoints by Sanger sequencing (Figure 2A and S2A). The breakpoint PCR confirmed that the *ATAD3* CNV arose via a *de novo* duplication event in 13 of the 13 families with available parental samples for comparison (Figure S2A). We detected no evidence of parental mosaicism for *ATAD3*dup in our cohort, although one patient (P7) had an older brother who died at six days of age with a suspicious clinical course (DNA unavailable for investigation).

Our extensive cohort supports a striking similarity between clinical presentations for *ATAD3*dup patients (Tables 1 and S1), with hypertrophic cardiomyopathy, hyperlactacidemia and perinatal death being nearly invariant features. Corneal clouding or cataracts, encephalopathy and white matter abnormalities were also common. Compared to the severe pontocerebellar hypoplasia observed in all *ATAD3*del patients, neurological findings in *ATAD3*dup patients appear milder, ranging from features consistent with hypoxic ischemia to mild pontocerebellar hypoplasia (P1). Two additional patients (P14 and P16) with consistent clinical features were subsequently confirmed to carry *ATAD3* duplications by breakpoint PCR. In total, we identified 17 patients from 16 families carrying recurrent

ATAD3 duplications of ~68 Kb with similar breakpoints spanning *ATAD3C*, *ATAD3B* and *ATAD3A*.

Sanger sequencing of the breakpoint PCR products spanning the *ATAD3A*/*ATAD3C* duplication junction identified six separate duplication breakpoints within this group of patients (Figure 2A and Table S2) that can be classified into four distinct duplication groups (Figure 2A, groups *a* - *d*). In keeping with the role of NAHR in rearrangements of the *ATAD3* locus[15] and those of other segmental duplications[8], the duplications occur in regions with extended stretches of significant homology between *ATAD3C* and *ATAD3A* (Table S2), with the homology in regions upstream from the breakpoints ranging from 93.5 – 99.3% identity over >950 bp in nearly all patients. The exception was P5, who had only 92.1% identity over 215 bp. However, due to the ethnic background of this patient (Mauritian), the reference genome and population databases may not accurately reflect all variation within this region and the stretch of homology may in reality extend further.

Expression of a chimeric ATAD3A/ATAD3C gene

The genomic architecture of the *ATAD3* locus for the four duplication groups predicts the generation of a chimeric *ATAD3A/ATAD3C* gene, as well as an extra copy of *ATAD3B*, in all cases (Figure 2B). This predicted architecture was further supported by Oxford Nanopore Technologies long read WGS from P3, which captured reads spanning the chimeric *ATAD3A/ATAD3C* gene (Figure S2B). The chimeric *ATAD3A/ATAD3C* genes are predicted to contain *ATAD3A* exons 1 through to 10–13 fused to *ATAD3C* exons 7–10 through to exon 12 (depending on the duplication group) (Figure 2B and Table S2). Using RNA isolated from patient fibroblast lines and heart samples, a stable chimeric *ATAD3A/ATAD3C* transcript (NM_001170535.1/NM_001039211.2) was detected in all patients studied that was absent from controls (Figure 3A, bottom panel). Stable *ATAD3A* and *ATAD3B* transcripts were expressed similarly to controls. The duplication was not predicted to alter the wild-type *ATAD3A* gene on the affected allele (Figure 2B). This was confirmed by Sanger sequencing of the *ATAD3A* transcript (Figure 3A, top panel), where heterozygous SNPs in the 3’ untranslated region of *ATAD3A* in all patients confirmed expression of both alleles.

As further confirmation of the predicted impact of the *ATAD3* duplication on transcripts, gene-specific qRT-PCR targeting the final exon boundaries was used to compare expression levels of the different *ATAD3* transcripts in patients versus controls (Figure 3B). *ATAD3A* levels were comparable between controls and *ATAD3*dup patients, consistent with the presence of two full-length copies of *ATAD3A*. *ATAD3*dup patients had a ~40–50% increase in *ATAD3B* transcript levels compared to controls, consistent with expression of a third, duplicated copy of *ATAD3B*. For validation, *ATAD3* transcript levels were also assessed in a previously reported *ATAD3*del patient (S4)[19], with a chimeric *ATAD3B*/*ATAD3A* gene expressed under the weaker *ATAD3B* promoter (Figure 1A). As expected, *ATAD3A* was ~60% reduced and *ATAD3B* levels were undetectable in the *ATAD3*del patient[19]. *ATAD3C*, which is normally expressed at low or negligible levels across all tissues, was virtually undetectable in cell lines from controls and *ATAD3*del patient S4 (Figure 3B and S3). However, in all *ATAD3*dup patients, transcripts corresponding to *ATAD3C* could be robustly detected at equivalent levels, confirming expression of the *ATAD3A*/*ATAD3C* chimeric gene under the *ATAD3A* promoter.

Robust confirmation that a stable protein is translated from the chimeric *ATAD3A*/*ATAD3C* gene is complicated by the lack of antibodies specific for each ATAD3 protein and the similarity of predicted molecular weights between ATAD3A (~66.2 kDa) and the chimeric ATAD3A/ATAD3C (~66.3 kDa) protein (Figure S4A-E). Therefore, label-free quantitative (LFQ) proteomics was performed on patient fibroblast lines to detect specific ATAD3 peptides and compare expression levels between patients and controls (Figure 3C-F). We initially analyzed two separate *ATAD3*del patients (S1a and S3; previously reported[19]), in whom the biallelic deletions were expected to result in expression of a chimeric protein 99.7% identical to ATAD3A, but expressed at a level similar to *ATAD3B* (Figure 1A). In support of this, the level of ATAD3A in the *ATAD3*del patients was ~25% of control levels (Figure 3D, left panel), equivalent to that of ATAD3B, with no differences in cytosolic GAPDH or mitochondrial VDAC1. In further confirmation of chimeric ATAD3B/ATAD3A protein expression, individual ATAD3B and ATAD3A specific peptides were mapped against the deleted region (Figure 3C). ATAD3B and ATAD3A specific peptides corresponding to the deleted region within the *ATAD3* locus were not detected in *ATAD3*del patients (Figure 3C), while all other ATAD3A specific peptides were detected at reduced frequency compared to controls (Figure 3D, right panel).

We next analyzed fibroblasts from three *ATAD3*dup patients (P3, P4 and P5; from duplication groups *b* and *c*). Supporting the qRT-PCR data (Figure 3B), ATAD3C specific peptides corresponding to the duplicated region of the gene were robustly detected in all *ATAD3*dup patients (P3, P4 and P5), but were undetectable in controls as well as the *ATAD3*del patients (Figure 3E-F and S4F). In all *ATAD3*dup patients, ATAD3C was detected at lower levels than ATAD3A, consistent with the expression of both the predicted chimeric ATAD3A/ATAD3C protein and two full length copies of ATAD3A (Figure 3F, left panel). Likewise, an increase was also observed for P4 in the abundance of ATAD3B, consistent with the extra copy found in *ATAD3*dup patients (Figure 3F, left panel), as well as increases in peptides specific to the duplicated *ATAD3A* region (Figure 3F, right panel). Similar analyses for P3 and P5 were constrained due to pooling of samples prior to analysis preventing evaluation of sample and control variability (Figure S4F). Altogether, the cDNA and proteomic data confirm the presence and stability of the chimeric ATAD3A/ATAD3C protein.

The effect of the ATAD3 duplication on oligomerization and mitochondrial function

Despite the different genomic coordinates of the duplication groups within the chimeric *ATAD3A*/*ATAD3C* gene architecture (Figure 2B), all were predicted to create an identical ATAD3A/ATAD3C chimeric protein since *ATAD3A* exons 11–13 and *ATAD3C* exons 7–9 have virtually identical reference sequences (Figure 4A and Table S2). The ATAD3A/ATAD3C chimera is 95.1% identical and 96.4% similar to ATAD3A. However, several of the canonical AAA-ATPase residues conserved within the ATAD3A ATPase domain[13,28] are altered in ATAD3C, including critical residues in the Sensor-I motif and the “arginine finger” involved in ATP hydrolysis[41].

AAA-ATPases typically function as homo- or heterohexameric oligomers[41], with both murine and human ATAD3 observed predominantly in a ~900 kDa complex, with a range of smaller complexes from ~250–900 kDa possibly corresponding to oligomeric ATAD3 structures[14,18,42]. To determine whether the expression of the chimeric ATAD3A/ATAD3C protein impeded ATAD3 complex assembly, we analyzed isolated mitochondria from control and *ATAD3*dup tissues and fibroblasts by blue native (BN)-PAGE, which enables separation of detergent solubilized intact protein complexes[43]. In mitochondria from control heart, liver and fibroblasts, we observed a similar distribution of ATAD3 complexes (~200–900 kDa) to those previously reported (Figure 4B and 4C). In most *ATAD3*dup mitochondrial samples, a prominent ~900 kDa complex was present that migrated at a slightly faster rate than the control ATAD3 complex. A similar alteration in the distribution of the ATAD3 complexes was observed in *ATAD3*dup patient heart mitochondria, despite inconsistencies in sample loading (Figure 4B). Unfortunately, there were apparent sample integrity issues with heart and liver biopsies from P6, possibly related to sub-optimal tissue collection (recorded as up to 24hrs postmortem), handling or storage. In contrast to the *ATAD3*dup patient samples, the ATAD3 complexes were nearly undetectable in mitochondria isolated from *ATAD3*del patient fibroblasts[19] (S3) (Figure 4C).

Examination of the stained BN-PAGE gel of mitochondria solubilized with the detergent digitonin (Figure 4B, bottom panel) showed an obvious decrease in the amount of OXPHOS supercomplexes in *ATAD3*dup patient heart and liver mitochondria compared to controls. However, no striking differences in OXPHOS complexes were seen in fibroblasts (Figure S5A, left panel), consistent with OXPHOS enzymology studies (Figure 4D). In all *ATAD3*dup patients with available heart biopsies, complex I (CI; NADH: ubiquinone oxidoreductase) activity was decreased to ~5% of normal control activity (Figure 4D and Table S3). Complex I activity was also decreased in *ATAD3*dup patient liver biopsies (~20% of control activity, Figure 4D) although this reduction was variable (Table S3). Complex IV (CIV; cytochrome *c* oxidase) activity was also somewhat decreased in liver and heart (~40% or ~58% of control activity, respectively). Decreased complex I and IV activity was also observed in some *ATAD3*dup patient muscle and fibroblast samples, however these tended to be less marked and were not considered diagnostically significant. Isolated complex I deficiency, or combined complex I and IV defects, are often observed in disorders of mtDNA replication and expression[44]. However, few of the patients had overt mtDNA depletion, nor were any found to have mtDNA deletions. The frequent increases in citrate synthase activity and mtDNA/nuclear DNA (nDNA) ratios observed are suggestive of mitochondrial proliferation (Tables S1 and S3).

Due to the structural alterations in OXPHOS supercomplex formation in isolated heart and liver mitochondria from the *ATAD3*dup patients (Figure 4B, bottom panel), as well as mitochondrial OXPHOS enzymology results, complex I assembly was analyzed. In mitochondria solubilized with Triton X-100 to separate the individual OXPHOS complexes, a strong reduction in assembled complex I was observed in heart and liver from all *ATAD3*dup patients (Figure 4E). Further analysis of the steady state levels of subunits from individual OXPHOS complexes in total heart extracts showed no detectable complex I subunit NDUFB8 in all *ATAD3*dup patients, and more modest reductions in complex III, IV and V subunits UQCRC2, MT-COX2, and ATP5A, respectively (Figure 4G). The decreased steady state protein levels correlated with OXPHOS complexes that contain mtDNA-encoded subunits, as no changes were observed in complex II subunit SDHB, nor mitochondrial proteins VDAC1/porin (outer mitochondrial membrane) and ANT3 (inner mitochondrial membrane). Additional analysis of complex III assembly in heart and liver mitochondria indicated a subtle increase in the dimeric complex in patients compared to controls (Figure S5B). In contrast, no complex I defect was detected in *ATAD3*dup patient fibroblasts (Figure 4F and S5A, right panel), nor was complex III or IV assembly affected (Figure S5C). This was consistent with quantitative proteomic analysis of fibroblasts from patient P4 (Figure S5D).

Discussion

ATAD3, a hotspot for genomic variation and pathogenic CNVs

Pediatric mitochondrial disease, including lethal perinatal presentations, is most often thought to have autosomal recessive inheritance[1]. The *de novo* nature of *ATAD3* duplications markedly alters the reproductive landscape for families, with the recurrence risk estimated to be 1 – 4% for gonadal mosaicism[45] rather than 25%. The identification of these recurrent pathogenic duplications and other *ATAD3* variants is also shifting the genomic landscape of mitochondrial diagnostics. In our experience of providing genomic diagnoses of mitochondrial disease to more than 500 children from Australia and New Zealand, the *ATAD3* locus is now among the five most common nuclear gene causes (Figure 5A). Given all our *ATAD3* patients died in the perinatal period, *ATAD3* now appears to be the most common gene locus underlying lethal perinatal mitochondrial disease. The four other common genes, all identified ~20–30 years ago[46], are prominent within our patient cohort due to common recessive European founder variants (*POLG* and *SURF1*)[47,48] or due to the vagaries of X chromosomal inheritance (*PDHA1* and *TAZ*). The absence of common European *POLG* founder mutations in populations such as Japan means that *POLG* disorders are less common there[49]. Significantly, the *ATAD3* region is the only known locus underlying mitochondrial disease in which segmental duplications lead to recurrent NAHR events. During the preparation of this manuscript, Gunning *et al*[20] reported five additional *ATAD3*dup patients carrying two of the six *de novo* breakpoints we describe here ("*a*" and "*b*" type duplications). Therefore, 48 *ATAD3* patients (39 families) have now been reported since 2016, including 37 with recurrent SNV or CNV mutations (Figure 5B).

Many of the patients in this study underwent multiple rounds of genetic and genomic investigations and reanalysis over many years before the *ATAD3* duplication was identified. In this cohort, analysis of coverage depth from WGS and WES data proved highly reliable, indicating retrospective analysis of existing sequencing data would readily identify affected individuals. However, it is important to note that microarrays are inefficient at detecting *ATAD3* duplications (two of six patients by high-density SNP-array, Figure S1C; two of three patients by custom array-CGH[20]) and are thus not suited for molecular diagnosis. The software for CNV detection relies on both LogR detection of probe intensity as well as an indication of allelic imbalance from detection of several contiguous B allele values. This can be complicated for duplications, particularly those within segmental duplications, and the detection can be affected by probe sensitivity, allele frequency and DNA quality[38].

Therefore, it is not surprising that only one *ATAD3*dup patient was identified in the in-house (VCGS) microarray database over the last 13 years. Many of the analyses were performed on prenatal samples or products of conception (~18,000 since 2014), so *ATAD3* duplications may underlie additional unsolved deaths *in utero*.

Reciprocal ATAD3 deletions and duplications

The *ATAD3* locus resembles other chromosomal "hot spots" with genomic instability due to repetitive sequences[50,51], many of which are now linked to genomic disorders[8,9]. Analysis of repeat regions across the *ATAD3* locus indicates multiple regions of ≥900 bp of high identity, a subset of which correspond to all reported pathogenic *ATAD3* deletion and duplication breakpoints (Figure 5C). The location of these breakpoints is likely explained by the length and identity of homologous low-copy repeat pairs, the GC content and the density of the PRDM6 recombination hot spot motif[8,10,52]. Indeed, it has been noted that low-copy repeat pairs flanking frequent recurrent *de novo* deletions share >98% DNA identity[10]. Since the reported pathogenic *ATAD3* duplications and deletions, as well as other CNVs, all arise from the same process (Figure 1A) they would be expected within the population if viable. However, more research is needed to fully define pathogenic versus non-pathogenic *ATAD3* variation, as this is complicated by the genomic complexity of the region which makes it difficult to uniquely map reads and clarify breakpoints.

The clinical presentations of all reported *ATAD3*dup patients are remarkably consistent (Figure 5D). While cardiomyopathy and severe pontocerebellar hypoplasia largely distinguish the *ATAD3*dup and *ATAD3*del cohorts, many other clinical features are shared. Nonetheless, the mechanisms behind the genotype-phenotype correlations are not yet clear and some patients with *ATAD3A* SNVs have both cardiomyopathy and pontocerebellar abnormalities[15,18,19]. Importantly, the striking clinical consistency of the *ATAD3*dup phenotype enabled us to readily identify candidate patients from our mitochondrial disease cohorts (Figure 2A, P14 and P16) by searching for similar clinical presentations, with the caveat that patients with divergent presentations would have been overlooked.

Unsurprisingly, the *ATAD3*dup is absent from gnomAD-SV[53] and was identified in only a single patient in DECIPHER[54], corresponding to *ATAD3*dup subject 5[20]. The *ATAD3* locus itself is encompassed within the region associated with chromosome 1p36 deletion syndrome (MIM: 607872). One of the most common terminal deletion syndromes, monosomy 1p36 is phenotypically variable, often associated with neurodevelopmental delay and a variety of congenital abnormalities[55,56]. Numerous genes have been implicated in the variable phenotypes[55], the majority of which appear highly intolerant of haploinsufficiency[57]. It is unlikely that monoallelic loss of *ATAD3* would contribute to this syndrome, with no constraint against *ATAD3A*, *ATAD3B* and *ATAD3C* loss of function variants, and *ATAD3*del carriers appearing normal[19,57].

In contrast, only a few patients with exclusive 1p36.3 duplications/triplications have been reported, with milder, variable features usually including global developmental delay or intellectual disability[58]. While the overall contribution of increased *ATAD3* gene dosage to these phenotypes is unclear, an increase of ATAD3B and/or ATAD3C alone would likely play a limited role, with Gunning *et al.* noting numerous apparently benign *ATAD3* specific duplications within DECIPHER that do not involve *ATAD3A*[20]. Overall, this supports the idea that increased *ATAD3B* gene dosage does not contribute to the severe pathogenicity of the *ATAD3*dup. Instead it appears more likely that the pathogenicity is related to expression of the chimeric ATAD3A/ATAD3C protein. Furthermore, increased ATAD3 levels alone do not specifically correlate with cardiac abnormalities, with atrial septal defects or left ventricular hypertrophy only observed in three of the eight 1p36.3 duplication patients[58], and one of the 23 duplications completely overlapping *ATAD3* reported in the DECIPHER database.

Complex I deficiency, mtDNA homeostasis and ATAD3

The most common biochemical defect detected in pediatric mitochondrial disease is isolated complex I deficiency, accounting for about one third of all cases[59]. Severe complex I deficiency was observed in all eight *ATAD3*dup patients with available heart tissue (Table S3). In fact, six of these *ATAD3*dup patients were investigated as part of a cohort of 103 complex I deficient mitochondrial disease patients[60]. The identification of the *ATAD3* duplication provides a genetic diagnosis for a further 6% of the patients within that cohort. At the time (2010), patients within the cohort with cardiac associated presentations had a poor molecular diagnostic rate (3/17, or 18%[60,61]). The *ATAD3* duplication now accounts for a further 29% of molecular diagnoses within this group of cardiac patients with isolated complex I deficiency (5/17).

Complex I deficiency was also observed in muscle-specific *Atad3* knockout mice[42]. The impact on OXPHOS function could potentially be explained by issues with mtDNA stability or expression, and in the mouse model, progressive impairments in mtDNA replication and mtDNA depletion were observed[42]. ATAD3 has been connected with both the maintenance and membrane association of mtDNA nucleoids[22,27,28], and abnormalities in mtDNA nucleoids were observed in *ATAD3*del and *ATAD3*dup patient fibroblasts[19,20]. Since *ATAD3*dup patients also showed milder changes in OXPHOS complexes IV and V, disturbances in mtDNA homeostasis or expression could be causative of these defects. Isolated complex I deficiency is often observed in disorders affecting mtDNA replication or expression[62], most likely due to the large number of complex I subunits encoded by mtDNA[44]. Nevertheless, there is a lack of consistent evidence for mtDNA depletion in this group of *ATAD3*dup patients across tissues (Table S3), suggesting that the decreased levels of mtDNA observed in some patients might be secondary. In addition, the OXPHOS complexes, through their interaction in supercomplexes, show interdependence for their stability and therefore effects on one complex may secondarily affect others[63].

An alternative explanation for the impact on complex I and other OXPHOS complexes could instead be changes in mitochondrial membrane architecture or homeostasis. In mice, the complete loss of ATAD3 is embryonic lethal at a point when embryonic development involves rapid biogenesis of mitochondria to support increasing energy demands[14]. Reduced mitochondrial mass was observed in muscle fibers and bone marrow cells from the muscle-specific mouse *Atad3* knockout[42], as well as in *C. elegans* following *Atad-3* knockdown[13]. A similar loss of mitochondria was observed in flies expressing the dominant ATAD3A p.(Arg528Trp) variant and in the hematopoietic-specific mouse *Atad3* knockout, with both involving a concomitant increase in autophagy[15,34]. Evidence for increased autophagy has been observed in fibroblasts from several *ATAD3A* patients[15,16], as well as *ATAD3*dup patient P16 (Table S1). This increase could be a secondary response to cellular stress induced by ATAD3-mediated mitochondrial changes, and no real evidence of mitochondrial mass reductions was observed in tissues from *ATAD3*dup patients, based on mtDNA, enzymatic and proteomic measurements.

Many of the changes in mitochondrial biogenesis and structure may relate to the correlation between ATAD3 and lipid homeostasis. ATAD3A co-purifies with proteins involved in lipid metabolism, has been implicated in both steroid and lipid biosynthesis, and has been shown to facilitate mitochondria/endoplasmic reticulum contacts to support lipid transfer between the organelles[23,25–27]. This may involve channeling of cholesterol, a key building block in steroidogenesis, into mitochondria where it forms membrane domains that facilitate mtDNA nucleoid replication[12,22]. Defects in cholesterol homeostasis and mtDNA nucleoid architecture have been observed in both *ATAD3*dup and *ATAD3*del patient fibroblasts and may contribute to their clinical presentation[19,20].

Mechanisms of ATAD3dup pathogenicity

AAA ATPases are involved in many cellular processes, including DNA replication and protein disassembly, disaggregation and proteolysis[41]. However, unlike many other AAA ATPases involved in mitochondrial quality control at the inner membrane (e.g. AFG3L2 and SPG7), ATAD3 does not have a proteolytic domain[21,64]. AAA ATPases typically form hexamers that perform coordinated ATP hydrolysis, with catalysis in one subunit often triggering conformational changes in the next subunit such that progressive ATP hydrolysis occurs within the oligomer[48]. ATAD3A has conserved AAA ATPase domains, including the Walker A and Walker B motifs required for ATP binding and hydrolysis, as well as Sensor I and II, and arginine finger motifs required for cooperative ATP hydrolysis[65] (Figure 4A). The dominant ATAD3A p.(Gly355Asp) Walker A mutation causing spastic paraplegia inhibits ATPase activity[16] (Figure 5B). ATAD3C, encoded by a proposed pseudogene[15], lacks key Sensor I and arginine finger residues (Figure 4A and [20]) and has yet to be confirmed as integral to mitochondrial membranes. Both the Sensor I and arginine finger domains of AAA ATPases are highly intolerant of substitution, with the arginine finger residue interacting in *trans* with the γ phosphate of ATP bound to the neighboring subunit[65].

While AAA ATPases can form homo- or heterocomplexes, the composition of ATAD3 oligomers is unclear due to non-specificity of ATAD3 antibodies, and could theoretically include a combination of ATAD3C, ATAD3B, or ATAD3A molecules. In *ATAD3*dup patients, it seems that expression of chimeric ATAD3A/ATAD3C interferes with normal ATAD3 oligomerization, likely inhibiting ATPase activity due to the changes in critical residues of the AAA ATPase domain of the protein (Figure 4). Intriguingly, dimerization of ATAD3A reportedly relies on the N-terminal coiled-coil domain[11,12,33], which is not altered in the chimeric ATAD3A/ATAD3C protein. Therefore, the observed changes in ATAD3 oligomerization in *ATAD3*dup patients likely result from inhibited ATP hydrolysis. Nonetheless, it is unclear why severe OXPHOS changes were observed primarily in heart despite similar changes to ATAD3 oligomerization observed in all tissues studied. Relative amounts of ATAD3A to ATAD3B may play a role, with ATAD3B shown to both co-purify with ATAD3A and proposed to negatively regulate ATAD3A interaction with mtDNA nucleoids[11]. Predictions of ATAD3 complex composition in *ATAD3*dup patients estimate that ~91% of hexamers would contain at least one chimeric ATAD3A/ATAD3C molecule[20]. However, the calculations do not take ATAD3B into account and tissue specific differences in ATAD3 ratios could potentially contribute to differences in tissue specificity and clinical presentation between the *ATAD3*dup and *ATAD3*del patients. Notably, while *ATAD3A* expression is relatively consistent across brain regions, *ATAD3B* expression is markedly higher in cerebellum (Figure S3A and S3B). *ATAD3*del patients express an ATAD3A-like protein under the *ATAD3B* promoter (Figure 1A) and this alteration in ratios could contribute to the severe pontocerebellar hypoplasia observed in these patients but not in most *ATAD3*dup patients.

Summary

We have identified recurrent *de novo* duplications in the *ATAD3* locus that lead to expression of a chimeric ATAD3A/ATAD3C protein, resulting in a characteristic phenotype that includes perinatal lethal mitochondrial hypertrophic cardiomyopathy with tissue-specific isolated complex I deficiency. The remarkable clinical consistency and the ability to discern the duplications on WES and WGS means patients can be readily identified, even from retrospective data, and families advised as to the low recurrence risk. Furthermore, *ATAD3*dup patients present with intriguing changes to ATAD3 oligomerization that point to a role for ATAD3 interaction and its ATPase function in the disease pathomechanism.

Limitations of Study

Most of the patients with *ATAD3* duplications we identified were from retrospective cohorts. The distinctive clinical phenotype led to ascertainment of additional cases based on testing of patients with similar symptoms. Hence the range of clinical phenotypes caused by *ATAD3* duplications may be broader than we identified, as exemplified by the single patient within our *ATAD3*dup cohort that did not have obvious cardiomyopathy. As well, the data imply that the ATAD3A/ATAD3C fusion protein is the primary, dominant cause of mitochondrial dysfunction rather than the extra copy of ATAD3B. Given the tissue specificity of the clinical and biochemical defect, more definitive proof would need carefully titrated expression studies in a cardiomyocyte cell line. These observations underscore the need for further clarification of the molecular mechanisms of ATAD3 in mitochondrial biogenesis, pathogenic versus non-pathogenic ATAD3 variation, and tissue specific determination of the individual contribution and interactions between ATAD3C, ATAD3B, and ATAD3A.

STAR Methods

RESOURCE AVAILABILITY

Lead Contact—Further information and requests for resources and reagents should be directed to and will be fulfilled by the Lead Contact, David Thorburn (david.thorburn@mcri.edu.au).

Materials Availability—There are restrictions to the availability of the patient cell lines/ tissues/genetic material described in this manuscript due to ethics and patient/family consent. Requests directed to the Lead Contact will be considered on an individual basis.

Data and Code Availability—Original/source data for Figures 2, 3 and 4, including gels, western blots, qRT-PCR data and associated supplemental data, is available through the Lead Contact. The published article includes proteomics datasets generated and analyzed during this study.

There are restrictions to the availability of genomics and microarray datasets used in this publication due to patient privacy and ethical restrictions. Any requests should be directed to the Lead Contact.

EXPERIMENTAL MODEL AND SUBJECT DETAILS

Subjects—Patient samples were obtained with familial informed consent as part of diagnostic investigations, and associated studies were approved by the respective institutional human research ethics boards. The overall study was approved by the Royal Children's Hospital Institutional Review Board (HREC reference numbers 34228, 36291, and 36378). Brief descriptions of the 17 affected individuals (from 16 families) are provided in Table 1, with more detailed clinical information available in Table S1.

Cell culture—Patient fibroblasts generated from skin biopsies were grown at 37°C and 5% CO_2 in Dulbecco's modified Eagle's medium (DMEM; Invitrogen, Carlsbad, CA) supplemented with 10% (v/v) fetal bovine serum (FBS, Invitrogen).

METHOD DETAILS

Genomic sequencing and CNV detection—DNA from individuals was extracted from blood, fibroblasts and tissues and investigated through whole exome sequencing (WES) with clinical or targeted analysis, whole genome sequencing (WGS), 10x Genomics Chromium linked-read WGS, Oxford Nanopore Technologies long read WGS and microarrays.

Trio WGS was performed on individual P1 and her parents by IIlumina Cambridge Ltd on an Illumina HiSeq X Ten with 2 × 150 bp reads and minimum mean coverage depth of 37x. For patients P2b and P3, singleton WGS was performed at the Kinghorn Centre for Clinical Genomics, also on Illumina HiSeq X Ten sequencers with 2 × 150 bp reads and >30x mean nuclear coverage. For these patients, sequences were aligned to the b37d5 human reference genome using BWA-mem[68]. Single nucleotide variants (SNVs) and small insertions/ deletions (indels) were called using GATK HaplotypeCaller (v3.7.2)[69] while copy number variants (CNVs) were called for P1 using canvas SPW[70] and variant annotation was performed using SnpEff v4.3m3[71] and custom scripts were used for variant filtration and prioritization. For P2b and P3, variants were annotated using ENSEMBL's VEP (v74)[72] and converted to an SQLite database using Gemini (v0.11.0 and v0.17.2, respectively)[73]. Gemini databases were imported into Seave[74] for variant filtering and prioritization. Mitochondrial (mt)DNA SNV and indel analysis was performed using Mity[75], while structural variants (both nuclear and mtDNA) were identified using ClinSV (Minoche et al, *manuscript in* *preparation*), which combines Lumpy[76] and CNVnator[35] to look for discordantly mapping read pairs, split-mapping reads and depth of coverage changes.

Six individuals, P4-P9, formed part of a previously assembled cohort of complex I deficiency patients (DT24, DT98, DT86, DT106, DT93 and DT101, respectively[60]). Their DNA underwent singleton WES with targeted analysis of 2,273 mitochondrial and differential diagnosis genes at the Broad Institute of MIT and Harvard as published (per patient 1 in [77]). Analysis of mtDNA for SNVs, indels and large deletions was performed as described previously[78]. Sequencing data for this targeted gene set were also analyzed for large CNVs using ExomeDepth (v.1.1.6)[36], with a reference set compiled using sequence data from 92 individuals generated by identical laboratory and computational procedures.

Individuals P10–13 and P14 underwent clinical WES at Juntendo University, Saitama Medical University and the Victorian Clinical Genetics Services, respectively. For P10–13, exomes were captured using SureSelect V5 (for P10) or TruSeq (for P11–13) exome enrichment kits (Agilent Technologies) according to the manufacturers' protocols. Sequencing was performed using 2 × 150 bp reads on an Illumina HiSeq2500 (for P10) or GAIIx (for P11–13). Whole-exome sequencing was performed using methods and a bioinformatic filtering pipeline as previously published[79]. The CNV analysis was performed on whole exome sequencing data using XHMM[37] (eXome-Hidden Markov Model) and ExomeDepth[36] with default parameters, and the detected CNVs were visualized using R software. For P14, the library was prepared using an Agilent SureSelect QXT CREv1 kit and sequenced on an Illumina HiSeq 4000 sequencer with a targeted mean coverage of 100x and a minimum of 90% of bases sequenced to at least 15x. Data was processed using Cpipe[80] with analysis of SNVs and indels in nuclear and mtDNA-encoded genes as well as large mtDNA deletions performed as per[81], and for CNVs within the nuclear genome using Ximmer[82], which combines CNV callers XHMM[37], ExomeDepth[36] and CODEX[83].

Genomic DNA was extracted from fibroblasts using Nucleobond CB20 for P3, P4, P5 and P8 for 10x Genomics Chromium linked-read WGS (performed at the Victorian Clinical Genetics Services), and was assessed by Qubit (ds DNA High Sensitivity kit) and Agilent TapeStation genomic DNA kits prior to library preparation using the Chromium™ Genome Chip Kit v2 as per manufacturer's genome protocol (10x Genomics, Pleasanton, CA, USA) and barcoded using the Chromium Controller (10x Genomics). DNA samples were partitioned into gel bead-in-emulsion (GEMs), with the introduction of 16 bp 10x barcodes (bead barcode), 10 bp unique molecular identifiers (UMI), and sample-specific 8 bp barcodes onto the DNA fragments and sequencing library preparation occurring in parallel. Library yield and fragment sizes were determined using an Agilent TapeStation D1000 kit (Agilent, Santa Clara, CA, USA). The barcoded libraries were sequenced on an Illumina NovaSeq 6000 system (paired-end 2× 150 bp). The resulting BCL files were demultiplexed and converted to FASTQ files using bcl2fastq2 (v2.20.0.422). Linked-reads were aligned to the GRCh37/hg19 reference genome using the LongRanger (v2.2.2) pipeline[84] to allow structural variant (SV) discovery.

Long-read Whole Genome Sequencing (WGS)—Long-read WGS using Oxford Nanopore Technologies (ONT) was performed to further validate the configuration of the breakpoint in P3. The gDNA isolated using Nucleobond CB20 was prepared using the 1D ligation library prep kit (SQK-LSK109) as per manufacturer's instructions, using 1500ng input DNA for DNA repair and end-prep and 1000ng end-prep DNA for adaptor ligation. 600ng of adaptor ligated DNA library were sequenced on a PromethION flow cell (FLO-PRO002). Real time data acquisition and base calling were performed using MinKNOW ID 19.06.8 and Guppy v3.0.04. To visualize reads mapping across the duplicated region of the *ATAD3* locus, an artificial version of the hg19 chr1 reference sequence was generated by duplicating the sequence in region chr1:1392271–1460342. ONT sequence reads marked as "pass" by Guppy were mapped to the artificial chr1 reference sequence using minimap2 (version 2.17)[85] using settings "-ax map-ont -t 4 -MD". R (version 3.5.0) and the Bioconductor Gviz package (version 1.24.0)[86] were used to visualize aligned reads with a mapping quality larger than 0 and read length no less than 2 Kb.

SNP microarray—Chromosomal SNP microarrays were performed on P3, P4, P5, P7, P8 and P15 by the Victorian Clinical Genetics Services (VCGS) using Illumina Infinium Global Screening Array-24 (GSA) v2.0 BeadChips according to manufacturer's instructions (Illumina, San Diego, CA, USA) and analyzed by Illumina KaryoStudio v1.4.3.0 Build 37. The Infinium GSA-24 array has 16 probes across the region chr1:g.1,378,485–1,470,321 (GRCh37/hg19; six in *ATAD3A*, four each in *ATAD3B* and *ATAD3C,* and 2 intergenic).

Evaluation of CNV boundaries and breakpoints—Intragenic duplications were investigated by long-range PCR amplification using Expand long range dNTPack kit (Roche); primers used and their binding sites within the *ATAD3* region are shown in Table S4. Sanger sequencing of the PCR products was performed as described previously[60] to define the breakpoints.

Gene-specific RNA studies—To study the effect of the *ATAD3* duplication on mRNA expression and splicing, total RNA was extracted from cultured fibroblasts grown with or without cycloheximide treatment (to stabilize transcripts normally degraded via nonsense mediated decay) and cDNA was synthesized as described previously[60]. cDNA transcripts were amplified by long range PCR as described previously using indicated primers (Table S4). For qRT-PCR assays, RNA was isolated from three different culture plates for each fibroblast line using TRIzol RNA Isolation Reagents (Invitrogen) and then reverse-transcribed to cDNA using SuperScript IV First-Strand Synthesis System (Invitrogen) according to the manufacturer's instructions. Synthesized cDNA was used as a template in qRT-PCR performed in a Roche LightCycler 480 using Power SYBR Green PCR Master Mix (Applied Biosystems) with primer combinations specific for *ATAD3A*, *ATAD3B* or *ATAD3C* (Table S4), and analysis performed by $2^{-\Delta\Delta CT}$ method[87].

Genomic DNA and protein sequence analyses—Pairwise alignments and sequence comparisons of DNA and protein sequences were performed using EMBOSS Needle (https://www.ebi.ac.uk/Tools/psa/emboss_needle/)[88]. The Miropeats program (v2.02) was employed to compare and graphically display the homology between the three human *ATAD3* paralogs[67]. A threshold of 900 was set for intrachromosomal comparison of human paralogs.

Respiratory chain enzyme and mtDNA analyses—Spectrophotometric enzyme assays assessing mitochondrial oxidative phosphorylation (OXPHOS) and citrate synthase activities were performed in duplicate for samples from individuals P2a, P3–9, P14 and P16 in Melbourne and for P10–13 in Chiba, as described previously[89]. For heart, skeletal muscle and liver samples, post-nuclear supernatants were prepared at ~4°C by homogenizing 10 – 100 mg (wet weight) of tissue in 9 volumes of Tissue buffer (5 mM HEPES, 1 mM EGTA, 210 mM mannitol, 70 mM sucrose, pH 7.2) with 10 strokes in a glass–glass homogenizer followed by centrifugation at 600 RCF for 10 min. Supernatants were frozen and thawed three times and aliquots for citrate synthase and complex I assays were given 5 x 6 pulses at setting 3, 30% duty cycle on a Branson microtip sonifier. For cultured fibroblasts (four confluent 175 sq.cm. flasks), mitochondria were prepared at ~4°C by resuspending cell pellets in MegaFb buffer (250 mM sucrose, 2 mM HEPES, 0.1 mM EGTA, pH 7.4), followed by two rounds of Teflon/glass homogenization and centrifugation at 600 RCF for 10 min at 4°C. Supernatants from the two rounds were pooled and centrifuged for 10 min at 14,400 RCF and resuspended in 400 µl of MegaFb buffer. An aliquot was retained for assay of complex III and remaining sample was centrifuged for 10 min at 14,400 RCF and resuspended in 1ml of Hypotonic buffer (25 mM potassium phosphate, pH 7.2, 5 mM $MgCl_2$). After centrifugation at 14,400 RCF as before, pellets were resuspended in 300 µl of Hypotonic buffer and frozen and thawed three times.

Enzyme assays measured the change of absorbance in a 1 mL cuvette at 30 °C over 3 min in 50 mM potassium phosphate buffer, pH 7.4 using a Cary 300 Bio Spectrophotometer (Agilent Technologies Australia). Protein levels were measured using bicinchoninic acid (BCA) and enzyme activities were expressed as initial rates (nmol/min/mg) except for complexes III and IV, which were expressed as rate constants (/min/mg). Enzyme activities were expressed as % of the mean of at least 6 matrix-matched control samples.

Rotenone-sensitive complex I (NADH-CoQ_1 oxidoreductase) activity was assayed with 50 µM NADH, 1 mM KCN, 10 µM antimycin A, 0.1% (w/v) fatty acid free BSA, 50 µM coenzyme Q_1 (CoQ_1) with and without 2.5 µM rotenone (Absorbance 340 nm, mM extinction coefficient 6.81).

Complex II (succinate: CoQ_1 oxidoreductase) activity was assayed after 10 min pre-incubation with 10 mM sodium succinate, 1 mM KCN, 10 µM antimycin A, 2.5 µM rotenone following addition of 50 µM CoQ_1 (Absorbance 280 nm, mM extinction coefficient 12).

Complex III (decylbenzylquinol: cytochrome *c* oxidoreductase) activity was assayed with 1 mM n-dodecylmaltoside, 1 mM KCN, 2.5 µM rotenone, 0.1% (w/v) fatty acid free BSA, 100 µM decylbenzylquinol and 15 µM cytochrome *c*. The assay was terminated by addition of a few grains of L-ascorbic acid to the cuvette to fully reduce cytochrome *c*, prior to a final absorbance reading that was subtracted from each data point before creating a log plot against time to calculate a first-order rate constant from the slope (Absorbance 550 nm, mM extinction coefficient 18.7). A 10mM decylbenzylquinol stock solution was freshly prepared in ethanol each day by reducing 300 µl 10 mM decylbenzylquinone with ~5 mg of KBH_4 and 10 µl 0.1 M HCl. After vortexing and 3 min at room temperature, 12 µl 3 M HCl was added to stabilize the decylbenzylquinol and excess KBH_4 crystals were removed by brief centrifugation.

Complex IV (cytochrome *c* oxidase) activity was assayed with 15 μM reduced cytochrome *c* and the assay was terminated by addition of $K_3Fe(CN)_6$ to 1 mM to complete oxidation of cytochrome *c* prior to a final absorbance reading and calculation of a first-order rate constant (Absorbance 550 nm, mM extinction coefficient 18.7). Reduced cytochrome *c* was prepared weekly by adding a few grains of ascorbic acid to 0.5 ml 2 mM cytochrome *c*, with removal of excess ascorbic acid using a PD-10 Sephadex G-25 gel filtration column (Sigma). Prior to use each day, the absorbance at 550 and 565 nm was measured and the solution was discarded if the A_{550} / A_{565} was <6.

Citrate synthase activity was assayed with 0.1 mM 5,5’ -dithio-bis-(2-nitrobenzoic acid) (DTNB), 0.1 mM acetyl CoA with and without 0.1 mM oxaloacetic acid (pH adjusted to 7.4) (Absorbance 412 nm, mM extinction coefficient 13.6).

The relative abundance of mtDNA vs nDNA was tested in liver, cardiac or skeletal muscle biopsies from several patient vs control tissues, as described previously[90]. This quantitative PCR method compares the relative levels of mtDNA to nDNA using TaqMan probes directed against the *MT-ND1* gene to represent mtDNA and a single copy nuclear reference gene, *CFTR*. Results are calculated by the $2^{-\Delta\Delta CT}$ method[87] and are the means of at least two independent runs of triplicate measurements. % mtDNA/nDNA ratios are calculated relative to the mean of at least 6 matrix-matched control samples.

SDS- and Blue Native (BN)-PAGE—For preparation of protein extracts, heart biopsy sections were solubilized using Extraction buffer (1.5% n-Dodecyl-β-d-maltopyranoside, 25 mM HEPES and 100 mM NaCl) for 20 min on ice and then centrifuged at 16,000 rpm for 20 min at 4°C. Protein concentrations of the supernatants were determined by BCA analysis[91], and 2–5 μg of each sample was further solubilized in sodium dodecyl sulfate (SDS)/glycerol solubilization buffer (125mM Tris pH8.8, 40% glycerol, 4% SDS, 100mM DTT, 0.01% Bromophenol blue, protease inhibitor cocktail) and analyzed by SDS-PAGE as described previously[61].

Mitochondria were isolated from 20–50 mg heart or liver biopsies, or fibroblasts (~1.5 X 10^6 cells) using differential centrifugation as described[92], and protein concentration determined by BCA analysis. BN-PAGE was performed as described previously[43,92], using 30 μg of mitochondria isolated from tissue or cells and solubilized in 1% Triton X-100 or 1% Digitonin.

Immunoblotting—SDS-PAGE or BN-PAGE gels were transferred to polyvinylidene difluoride (PVDF) membrane and probed with primary antibodies against ATAD3[28], ANT3 (Abcam anti-SLC25A6, ab154007), SDHA/complex II 70 kDa subunit (for SDS-PAGE: Molecular Probes, A-11142; for BN-PAGE: Abcam, ab14715), Porin/VDAC1 (Abcam ab14734), Total OXPHOS Human WB Antibody Cocktail (Abcam, ab110411), complex I subunit NDUFA9 raised in-house[93], ATAD3A (Abnova, H00055210-D01), ATAD3B (Abnova, H00083858-B01P), Tim23 (BD Bioscience, 611223), V5 (Invitrogen, R960–25), Core1 (ThermoFisher, 459140) and Cox4 (Abcam, ab110261). Blots were incubated with anti-mouse or anti-rabbit IgG secondary antibodies (GE Healthcare) and developed with Clarity Western ECL Substrate (Bio-Rad Laboratories).

Protein expression and immunoprecipitation—ATAD3A (NM_001170535.3), ATAD3C (NM_001039211.3) and chimeric ATAD3A/ATAD3C (NM_001170535.3 exons1-exon11 + NM_001039211.3 exons8–12) were cloned into the CS-CA-MCS vector [obtained from Riken BRC DNA Bank, RDB05963 (deposited by Dr Hiroyuki Miyoshi)]. For co-immunoprecipitation studies, HEK293FT cells seeded at 2×10^6 cells in 6-cm plates were transfected with the indicated plasmids using Lipofectamine2000 (ThermoFisher Scientific) according to the manufacturer's protocols. Five days post-transfection, HEK293FT cells overexpressing ATAD3 were lysed for 10 min on ice with 0.15 ml of RIPA buffer (Nacalai Tesque, Inc), and the insoluble fraction was removed by centrifugation. The soluble fraction containing 100 μg protein was incubated with Protein G-Sepharose (Sigma) coated with anti-V5 antibody (Invitrogen). Immunoprecipitations were performed according to the manufacturer's guidelines.

Quantitative mass spectrophotometry—Mass spectrometry on primary fibroblast material was performed label-free, using sample preparation methodology previously described[77] with modifications. Fibroblasts from three to four different control subjects and two to three subcultures of patient cells were solubilized in 1% w/v sodium deoxycholate, 100 mM Tris-HCl (pH 8.1) and incubated at 99°C for 10 min with shaking. Samples were then incubated for 10 min at 60°C in a sonicator waterbath, followed by the addition of 5 mM Tris(2-carboxyethyl)phosphine, 20 mM chloroacetamide and incubation for 5 min at 99°C with shaking. Denatured and alkylated proteins were digested at 37°C overnight using MS grade trypsin (Thermo Scientific). Detergent was removed by extraction into ethyl acetate in the presence of 2% formic acid (FA) on SDB-RPS (styrenedivinylbenzene-reverse phase sulfonate; Supelco Analytical) stage-tips made in-house as described[94,95]. Peptides reconstituted in 0.5% FA were loaded onto small cation exchange (Empore Cation Exchange-SR, Supelco Analytical) stage-tips and the tips washed with 20% acetonitrile (ACN), 0.5% FA. Peptides were eluted over five fractions of increasing amounts (45–300 mM) of freshly prepared ammonium acetate in 20% ACN, 0.5% FA, followed by a final elution step using 80% ACN, 5% ammonium hydroxide. Fractions were concentrated by vacuum centrifugation and desalted on SDB-XC poly(styrene-divinyl-benzene; Supelco Analytical) stage-tips or Pierce C18 Spin Tips (Thermo Scientific) as per manufacturer instructions.

Peptides were reconstituted in 2% ACN, 0.1% trifluoroacetic acid and analyzed by online nano-HPLC/electrospray ionization-MS/MS on a Q Exactive Plus or Orbitrap Fusion Lumos connected to an Ultimate 3000 HPLC (Thermo-Fisher Scientific). For measurements of peptides derived from S1a, S3 and P4, analysis was performed on a Q Exactive Plus with chromatography conditions and instrument parameters as described previously[77]. Peptides were loaded onto a trap column (Acclaim PepMap C18 nano-trap column 75 μm x 2 cm, 3 μm particle size, 100 Å pore size; Thermo Fisher Scientific) at 5 μL/min in 2% (v/v) ACN containing 0.1% (v/v) FA for 3 min before switching the pre-column in line with the analytical column (Acclaim PepMap RSLC C18 analytical column 75 μm x 50 cm, 2 μm particle size, 100 Å pore size; Thermo Fisher Scientific). Separation of peptides was performed at 300 nL/min using a 120 min non-linear ACN gradient of buffer A [0.1% (v/v) FA, 2% (v/v) ACN, 5% DMSO] and buffer B [0.1% (v/v) FA in ACN, 5% DMSO]. The mass spectrometer was operated in positive-ionization mode with spray voltage set at 1.9 kV and source temperature at 275°C. Data were collected using the Data Dependent Acquisition (DDA) using m/z 350–1550 at 120000 resolution with AGC target of 5e5. The “top speed” acquisition method mode (3 sec cycle time) on the most intense precursor was used whereby peptide ions with charge states ≥2–5 were isolated with isolation window of 1.6 m/z and fragmented with high energy collision (HCD) mode with stepped collision energy of 30 ±5%. Fragment ion spectra were acquired in Orbitrap at 15000 resolution. Dynamic exclusion was activated for 30s. For P3 and P5, measurements were performed on an Orbitrap Fusion Lumos. Liquid chromatography (LC) coupled MS/MS was carried out on an Orbitrap Lumos mass spectrometer (ThermoFisher Scientific) with a nanoESI interface in conjunction with an Ultimate 3000 RSLC nanoHPLC (Dionex Ultimate 3000). The LC system was equipped with a trap column (Acclaim PepMap C18 nano-trap column 75 μm x 2 cm, 3 μm particle size, 100 Å pore size; Thermo Fisher Scientific) and an analytical column (Acclaim PepMap RSLC C18 analytical column 75 μm x 50 cm, 2 μm particle size, 100 Å pore size; Thermo Fisher Scientific). The tryptic peptides were injected into the trap column at an isocratic flow of 5 μL/min of 2% (v/v) CH3CN containing 0.1% (v/v) FA for 5 min applied before the trap column was switched in-line with the analytical column. The eluents were 5% DMSO in 0.1% v/v FA (solvent A) and 5% DMSO in 100% v/v CH3CN and 0.1% v/v FA (solvent B). The flow gradient was (i) 0–6min at 3% B, (ii) 6–95 min, 3–22% B (iii) 95–105min 22–40% B (iv) 105–110min, 40–80% B (v) 110–115min, 80–80% B (vi) 115–117min, 80–3% and equilibrated at 3% B for 10 minutes before the next sample injection.

The mass spectrometer was operated in positive-ionization mode with spray voltage set at 1.9 kV and source temperature at 275°C. The mass spectrometer was operated in the data-dependent acquisition mode MS spectra scanning from m/z 300–1600 at 120000 resolution with AGC target of 4e5. The “top speed” acquisition method mode (3 sec cycle time, 125 min run) on the most intense precursor was used whereby peptide ions with charge states ≥2–5 were isolated with isolation window of 0.7 m/z and fragmented with high energy collision (HCD) mode with stepped collision energy of 35 ±5%. Fragment ion spectra were acquired in Orbitrap at 50000 resolution. Dynamic exclusion was activated for 30s.

Raw files were analyzed using the MaxQuant platform ([96]; v.1.6.5.0) searching against the Uniprot human database containing reviewed canonical and isoform variants in FASTA format (June 2019) and a database containing common contaminants. Default search parameters for a label-free (LFQ) experiment were used with the following modifications “Deamidation (NQ)” was added as a variable modification, “Label-free quantification” option was set to “LFQ”, “LFQ min. ratio count” set to 1, “Label min. ratio count” set to 1, Match type “No matching” and “Peptides for quantification” set to “Unique”. Statistical analyses were performed using the Perseus platform ([97]; v.1.6.2.2). For the peptide heatmaps, peptides.txt files were loaded, and spurious identifications removed as above. “Normalized LFQ intensity” values were log2 transformed and entries containing “NaN” (indicating missing data) were replaced with zero. Heatmaps were generated using the built-in hierarchical clustering function in Perseus platform as above and only peptides that were detected in at least two samples shown. For the protein profile plots, columns and rows from the MaxQuant output file proteinGroups.txt were loaded and identifications annotated as “Only identified by site”, “Reverse”, and “Potential contaminant” were removed from the data. Following this, “Normalized LFQ intensity” values were log2 transformed and profile plots were generated using the built-in profile plot function. For the ATAD3 smoothed peptide plots, LFQ intensity values for missing peptides (NaN) were imputed with the lowest detected log2 value (16.2979 for S3; S1a; 16.7114 for P4) in each experiment, which represents the limit of detection for the instrumentation. The difference of the means was plotted using the geom_smooth function of ggplot2 library in RStudio (v. 3. 6. 2). The curve shows a loess smoothed curve with 95% confidence interval. Matrices for protein and peptide data are available in Tables S5 and S6, respectively.

QUANTIFICATION AND STATISTICAL ANALYSIS

Details of statistical details of experiments for qRT-PCR (Figure 3B), quantitative proteomics (Figure 3D and F) and respiratory chain enzymology (Figure 4D) can be found in the figures and/or figure legends. Analyses of qRT-PCR and respiratory chain enzymology data were performed using GraphPad Prism (v7.04). Analyses of quantitative proteomics data are detailed in the Methods section for “*Quantitative mass spectrophotometry*”.

Supplementary Material

Refer to Web version on PubMed Central for supplementary material.

Acknowledgements

We thank Meredith Wilson, Stefanie Eggers, Natalie Tan, Katherine Neas, Tegan Stait, Sabrina Kaminsky and Wendy Fagan for technical assistance, contributions to data collection, and/or clinical discussions. We appreciate the kind gifts of antibodies from Ian Holt and Antonella Spinazzola (anti-ATAD3) and Diana Stojanovski (anti-ANT3). We acknowledge the Melbourne Mass Spectrometry and Proteomics Facility (MMSPF) for provision of instrumentation, training, and technical support.

This research was supported by grants and fellowships from the Australian National Health and Medical Research Council (NHMRC) [1164479 (DRT, JC, DAS, AGC); 1155244 (DRT); 1068278 (CS); 1140851 (DAS)], the US Department of Defense Congressionally Directed Medical Research Programs PR170396 (DRT, JC, MTR, DAS), the New South Wales Office of Health and Medical Research Council Sydney Genomics Collaborative grant (JC), the Victorian Government’s Operational Infrastructure Support Program (DRT, JC), the Australian Mito Foundation (AEF, AGC, CS, DRT, JC, DAS, DHH, MTR), the National Council on Science and Technology (CONACYT) (RR), the Vincent Chiodo Charitable Trust (DRT), the Angela Wright Bennett Foundation and the McCusker Charitable Foundation (GB), the US National Institutes of Health R35GM122455 (VKM), and the Howard Hughes Medical Institute Investigator Program (VKM). Diagnosis of two patients was supported by the Australian Genomics Health Alliance (JC, DRT, CS, GB), which is funded by the NHMRC (1113531) and the Medical Research Future Fund. This work was supported in part by the Practical Research Project for Rare/Intractable Diseases from the Japan Agency for Medical Research and Development, AMED (19ek0109273, 18ek0109177) to KM, AO and YO, the Program for an Integrated Database of Clinical and Genomic Information from AMED (19kk0205014, 18kk0205002) to YO, MEXT-Supported Program for the Private University Research Branding Project, the Japan Society for the Promotion of Science (JSPS) KAKENHI 19H03624 (Grant-in-Aid for Scientific Research (B)) to YO and YK. The Genotype-Tissue Expression (GTEx) Project was supported by the Common Fund of the Office of the Director of the National Institutes of Health, and by NCI, NHGRI, NHLBI, NIDA, NIMH, and NINDS.

References

1. Gorman GS, Chinnery PF, DiMauro S, Hirano M, Koga Y, McFarland R, Suomalainen A, Thorburn DR, Zeviani M, and Turnbull DM (2016). Mitochondrial diseases. Nat Rev Dis Primers 2, 16080. [PubMed: 27775730]
2. Rahman J, and Rahman S. (2018). Mitochondrial medicine in the omics era. Lancet 391, 2560–2574. [PubMed: 29903433]
3. Stenton SL, and Prokisch H. (2018). Advancing genomic approaches to the molecular diagnosis of mitochondrial disease. Essays Biochem 62, 399–408. [PubMed: 29950319]
4. Stankiewicz P, and Lupski JR (2002). Genome architecture, rearrangements and genomic disorders. Trends Genet 18, 74–82. [PubMed: 11818139]
5. Bailey JA, Gu Z, Clark RA, Reinert K, Samonte RV, Schwartz S, Adams MD, Myers EW, Li PW, and Eichler EE (2002). Recent segmental duplications in the human genome. Science 297, 1003–1007. [PubMed: 12169732]
6. Pu L, Lin Y, and Pevzner PA (2018). Detection and analysis of ancient segmental duplications in mammalian genomes. Genome Res 28, 901–909. [PubMed: 29735604]
7. Lander ES, Linton LM, Birren B, Nusbaum C, Zody MC, Baldwin J, Devon K, Dewar K, Doyle M, FitzHugh W, et al. (2001). Initial sequencing and analysis of the human genome. Nature 409, 860–921. [PubMed: 11237011]
8. Carvalho CM, and Lupski JR (2016). Mechanisms underlying structural variant formation in genomic disorders. Nat Rev Genet 17, 224–238. [PubMed: 26924765]
9. Mefford HC, and Eichler EE (2009). Duplication hotspots, rare genomic disorders, and common disease. Curr Opin Genet Dev 19, 196–204. [PubMed: 19477115]
10. Dittwald P, Gambin T, Szafranski P, Li J, Amato S, Divon MY, Rodriguez Rojas LX, Elton LE, Scott DA, Schaaf CP, et al. (2013). NAHR-mediated copy-number variants in a clinical population: mechanistic insights into both genomic disorders and Mendelizing traits. Genome Res 23, 1395–1409. [PubMed: 23657883]
11. Merle N, Féraud O, Gilquin B, Hubstenberger A, Kieffer-Jacquinot S, Assard N, Bennaceur-Griscelli A, Honnorat J, and Baudier J. (2012). ATAD3B is a human embryonic stem cell specific mitochondrial protein, re-expressed in cancer cells, that functions as dominant negative for the ubiquitous ATAD3A. Mitochondrion 12, 441–448. [PubMed: 22664726]
12. Gilquin B, Taillebourg E, Cherradi N, Hubstenberger A, Gay O, Merle N, Assard N, Fauvarque MO, Tomohiro S, Kuge O, et al. (2010). The AAA+ ATPase ATAD3A controls mitochondrial dynamics at the interface of the inner and outer membranes. Mol. Cell. Biol 30, 1984–1996. [PubMed: 20154147]
13. Hoffmann M, Bellance N, Rossignol R, Koopman WJ, Willems PH, Mayatepek E, Bossinger O, and Distelmaier F. (2009). C. elegans ATAD-3 is essential for mitochondrial activity and development. PLoS One 4, e7644.
14. Goller T, Seibold UK, Kremmer E, Voos W, and Kolanus W. (2013). Atad3 function is essential for early post-implantation development in the mouse. PLoS One 8, e54799.
15. Harel T, Yoon WH, Garone C, Gu S, Coban-Akdemir Z, Eldomery MK, Posey JE, Jhangiani SN, Rosenfeld JA, Cho MT, et al. (2016). Recurrent De Novo and Biallelic Variation of ATAD3A, Encoding a Mitochondrial Membrane Protein, Results in Distinct Neurological Syndromes. Am J Hum Genet 99, 831–845. [PubMed: 27640307]
16. Cooper HM, Yang Y, Ylikallio E, Khairullin R, Woldegebriel R, Lin KL, Euro L, Palin E, Wolf A, Trokovic R, et al. (2017). ATPase-deficient mitochondrial inner membrane protein ATAD3A disturbs mitochondrial dynamics in dominant hereditary spastic paraplegia. Hum Mol Genet 26, 1432–1443. [PubMed: 28158749]
17. Peeters-Scholte CMPCD, Adama van Scheltema PN, Klumper F, Everwijn SMP, Koopmans M, Hoffer MJV, Koopmann TT, Ruivenkamp CAL, Steggerda SJ, van der Knaap MS, et al. (2017). Genotype-phenotype correlation in ATAD3A deletions: not just of scientific relevance. Brain 140, e66.
18. Peralta S, González-Quintana A, Ybarra M, Delmiro A, Pérez-Pérez R, Docampo J, Arenas J, Blázquez A, Ugalde C, and Martín MA (2019). Novel ATAD3A recessive mutation associated to

fatal cerebellar hypoplasia with multiorgan involvement and mitochondrial structural abnormalities. Mol Genet Metab 128, 452–462. [PubMed: 31727539]

19. Desai R, Frazier AE, Durigon R, Patel H, Jones AW, Dalla Rosa I, Lake NJ, Compton AG, Mountford HS, Tucker EJ, et al. (2017). ATAD3 gene cluster deletions cause cerebellar dysfunction associated with altered mitochondrial DNA and cholesterol metabolism. Brain 140, 1595–1610. [PubMed: 28549128]
20. Gunning AC, Strucinska K, Munoz Oreja M, Parrish A, Caswell R, Stals KL, Durigon R, Durlacher-Betzer K, Cunningham MH, Grochowski CM, et al. (2020). Recurrent De Novo NAHR Reciprocal Duplications in the ATAD3 Gene Cluster Cause a Neurogenetic Trait with Perturbed Cholesterol and Mitochondrial Metabolism. Am J Hum Genet 106, 272–279. [PubMed: 32004445]
21. Baudier J. (2018). ATAD3 proteins: brokers of a mitochondria-endoplasmic reticulum connection in mammalian cells. Biol Rev Camb Philos Soc 93, 827–844. [PubMed: 28941010]
22. Gerhold JM, Cansiz-Arda S, Lõhmus M, Engberg O, Reyes A, van Rennes H, Sanz A, Holt IJ, Cooper HM, and Spelbrink JN (2015). Human Mitochondrial DNA-Protein Complexes Attach to a Cholesterol-Rich Membrane Structure. Sci Rep 5, 15292. [PubMed: 26478270]
23. Issop L, Fan J, Lee S, Rone MB, Basu K, Mui J, and Papadopoulos V. (2015). Mitochondria-associated membrane formation in hormone-stimulated Leydig cell steroidogenesis: role of ATAD3. Endocrinology 156, 334–345. [PubMed: 25375035]
24. Poston CN, Krishnan SC, and Bazemore-Walker CR (2013). In-depth proteomic analysis of mammalian mitochondria-associated membranes (MAM). J Proteomics 79, 219–230. [PubMed: 23313214]
25. Hung V, Lam SS, Udeshi ND, Svinkina T, Guzman G, Mootha VK, Carr SA, and Ting AY (2017). Proteomic mapping of cytosol-facing outer mitochondrial and ER membranes in living human cells by proximity biotinylation. Elife 6, 10.7554/eLife.24463.24001.
26. Rone MB, Midzak AS, Issop L, Rammouz G, Jagannathan S, Fan J, Ye X, Blonder J, Veenstra T, and Papadopoulos V. (2012). Identification of a dynamic mitochondrial protein complex driving cholesterol import, trafficking, and metabolism to steroid hormones. Mol Endocrinol 26, 1868–1882. [PubMed: 22973050]
27. He J, Cooper HM, Reyes A, Di Re M, Sembongi H, Litwin TR, Gao J, Neuman KC, Fearnley IM, Spinazzola A, et al. (2012). Mitochondrial nucleoid interacting proteins support mitochondrial protein synthesis. Nucleic Acids Res 40, 6109–6121. [PubMed: 22453275]
28. He J, Mao CC, Reyes A, Sembongi H, Di Re M, Granycome C, Clippingdale AB, Fearnley IM, Harbour M, Robinson AJ, et al. (2007). The AAA+ protein ATAD3 has displacement loop binding properties and is involved in mitochondrial nucleoid organization. J Cell Biol 176, 141–146. [PubMed: 17210950]
29. Li S, Bouzar C, Cottet-Rousselle C, Zagotta I, Lamarche F, Wabitsch M, Tokarska-Schlattner M, Fischer-Posovszky P, Schlattner U, and Rousseau D. (2016). Resveratrol inhibits lipogenesis of 3T3-L1 and SGBS cells by inhibition of insulin signaling and mitochondrial mass increase. Biochim Biophys Acta 1857, 643–652. [PubMed: 26968895]
30. van den Ecker D, Hoffmann M, Muting G, Maglioni S, Herebian D, Mayatepek E, Ventura N, and Distelmaier F. (2015). Caenorhabditis elegans ATAD-3 modulates mitochondrial iron and heme homeostasis. Biochem Biophys Res Commun 467, 389–394. [PubMed: 26427876]
31. Harel T, and Lupski JR (2018). Genomic disorders 20 years on-mechanisms for clinical manifestations. Clin Genet 93, 439–449. [PubMed: 28950406]
32. Fang HY, Chang CL, Hsu SH, Huang CY, Chiang SF, Chiou SH, Huang CH, Hsiao YT, Lin TY, Chiang IP, et al. (2010). ATPase family AAA domain-containing 3A is a novel anti-apoptotic factor in lung adenocarcinoma cells. J Cell Sci 123, 1171–1180. [PubMed: 20332122]
33. Zhao Y, Sun X, Hu D, Prosdocimo DA, Hoppel C, Jain MK, Ramachandran R, and Qi X. (2019). ATAD3A oligomerization causes neurodegeneration by coupling mitochondrial fragmentation and bioenergetics defects. Nat Commun 10, 1371. [PubMed: 30914652]
34. Jin G, Xu C, Zhang X, Long J, Rezaeian AH, Liu C, Furth ME, Kridel S, Pasche B, Bian XW, et al. (2018). Atad3a suppresses Pink1-dependent mitophagy to maintain homeostasis of hematopoietic progenitor cells. Nat Immunol 19, 29–40. [PubMed: 29242539]

35. Abyzov A, Urban AE, Snyder M, and Gerstein M. (2011). CNVnator: an approach to discover, genotype, and characterize typical and atypical CNVs from family and population genome sequencing. Genome Res 21, 974–984. [PubMed: 21324876]

36. Plagnol V, Curtis J, Epstein M, Mok KY, Stebbings E, Grigoriadou S, Wood NW, Hambleton S, Burns SO, Thrasher AJ, et al. (2012). A robust model for read count data in exome sequencing experiments and implications for copy number variant calling. Bioinformatics 28, 2747–2754. [PubMed: 22942019]

37. Fromer M, Moran JL, Chambert K, Banks E, Bergen SE, Ruderfer DM, Handsaker RE, McCarroll SA, O'Donovan MC, Owen MJ, et al. (2012). Discovery and statistical genotyping of copy-number variation from whole-exome sequencing depth. Am J Hum Genet 91, 597–607. [PubMed: 23040492]

38. Alkan C, Coe BP, and Eichler EE (2011). Genome structural variation discovery and genotyping. Nat Rev Genet 12, 363–376. [PubMed: 21358748]

39. Frazier AE, Holt IJ, Spinazzola A, and Thorburn DR (2017). Reply: Genotype-phenotype correlation in ATAD3A deletions: not just of scientific relevance. Brain 140, e67.

40. Newman S, Hermetz KE, Weckselblatt B, and Rudd MK (2015). Next-generation sequencing of duplication CNVs reveals that most are tandem and some create fusion genes at breakpoints. Am J Hum Genet 96, 208–220. [PubMed: 25640679]

41. Gates SN, and Martin A. (2020). Stairway to translocation: AAA+ motor structures reveal the mechanisms of ATP-dependent substrate translocation. Protein Sci 29, 407–419. [PubMed: 31599052]

42. Peralta S, Goffart S, Williams SL, Diaz F, Garcia S, Nissanka N, Area-Gomez E, Pohjoismaki J, and Moraes CT (2018). ATAD3 controls mitochondrial cristae structure in mouse muscle, influencing mtDNA replication and cholesterol levels. J Cell Sci 131.

43. Wittig I, Braun HP, and Schägger H. (2006). Blue native PAGE. Nat Protoc 1, 418–428. [PubMed: 17406264]

44. Fassone E, and Rahman S. (2012). Complex I deficiency: clinical features, biochemistry and molecular genetics. J Med Genet 49, 578–590. [PubMed: 22972949]

45. Wilkie AOM, and Goriely A. (2017). Gonadal mosaicism and non-invasive prenatal diagnosis for 'reassurance' in sporadic paternal age effect (PAE) disorders. Prenat Diagn 37, 946–948. [PubMed: 28686291]

46. Frazier AE, Thorburn DR, and Compton AG (2019). Mitochondrial energy generation disorders: genes, mechanisms, and clues to pathology. J Biol Chem 294, 5386–5395. [PubMed: 29233888]

47. Hakonen AH, Davidzon G, Salemi R, Bindoff LA, Van Goethem G, Dimauro S, Thorburn DR, and Suomalainen A. (2007). Abundance of the POLG disease mutations in Europe, Australia, New Zealand, and the United States explained by single ancient European founders. Eur J Hum Genet 15, 779–783. [PubMed: 17426723]

48. Wedatilake Y, Brown RM, McFarland R, Yaplito-Lee J, Morris AA, Champion M, Jardine PE, Clarke A, Thorburn DR, Taylor RW, et al. (2013). SURF1 deficiency: a multi-centre natural history study. Orphanet J Rare Dis 8, 96. [PubMed: 23829769]

49. Yamazaki T, Murayama K, Compton AG, Sugiana C, Harashima H, Amemiya S, Ajima M, Tsuruoka T, Fujinami A, Kawachi E, et al. (2014). Molecular diagnosis of mitochondrial respiratory chain disorders in Japan: focusing on mitochondrial DNA depletion syndrome. Pediatr Int 56, 180–187. [PubMed: 24266892]

50. Sharp AJ, Hansen S, Selzer RR, Cheng Z, Regan R, Hurst JA, Stewart H, Price SM, Blair E, Hennekam RC, et al. (2006). Discovery of previously unidentified genomic disorders from the duplication architecture of the human genome. Nat Genet 38, 1038–1042. [PubMed: 16906162]

51. Liu P, Carvalho CM, Hastings PJ, and Lupski JR (2012). Mechanisms for recurrent and complex human genomic rearrangements. Curr Opin Genet Dev 22, 211–220. [PubMed: 22440479]

52. Paigen K, and Petkov PM (2018). PRDM9 and Its Role in Genetic Recombination. Trends Genet 34, 291–300. [PubMed: 29366606]

53. Collins RL, Brand H, Karczewski KJ, Zhao X, Alföldi J, Khera AV, Francioli LC, Gauthier LD, Wang H, Watts NA, et al. (2019). An open resource of structural variation for medical and population genetics. bioRxiv 578674, 10.1101/578674.

54. Firth HV, Richards SM, Bevan AP, Clayton S, Corpas M, Rajan D, Van Vooren S, Moreau Y, Pettett RM, and Carter NP (2009). DECIPHER: Database of Chromosomal Imbalance and Phenotype in Humans Using Ensembl Resources. Am J Hum Genet 84, 524–533. [PubMed: 19344873]

55. Jordan VK, Zaveri HP, and Scott DA (2015). 1p36 deletion syndrome: an update. Appl Clin Genet 8, 189–200. [PubMed: 26345236]

56. Heilstedt HA, Ballif BC, Howard LA, Kashork CD, and Shaffer LG (2003). Population data suggest that deletions of 1p36 are a relatively common chromosome abnormality. Clin Genet 64, 310–316. [PubMed: 12974736]

57. Lek M, Karczewski KJ, Minikel EV, Samocha KE, Banks E, Fennell T, O'Donnell-Luria AH, Ware JS, Hill AJ, Cummings BB, et al. (2016). Analysis of protein-coding genetic variation in 60,706 humans. Nature 536, 285–291. [PubMed: 27535533]

58. Marquet V, Bourthoumieu S, Dobrescu A, Laroche-Raynaud C, and Yardin C. (2017). Familial 1p36.3 microduplication resulting from a 1p-9q non-reciprocal translocation. Eur J Med Genet 60, 583–588. [PubMed: 28811188]

59. Kirby DM, Crawford M, Cleary MA, Dahl HH, Dennett X, and Thorburn DR (1999). Respiratory chain complex I deficiency: an underdiagnosed energy generation disorder. Neurology 52, 1255–1264. [PubMed: 10214753]

60. Calvo SE, Tucker EJ, Compton AG, Kirby DM, Crawford G, Burtt NP, Rivas M, Guiducci C, Bruno DL, Goldberger OA, et al. (2010). High-throughput, pooled sequencing identifies mutations in NUBPL and FOXRED1 in human complex I deficiency. Nat Genet 42, 851–858. [PubMed: 20818383]

61. Calvo SE, Compton AG, Hershman SG, Lim SC, Lieber DS, Tucker EJ, Laskowski A, Garone C, Liu S, Jaffe DB, et al. (2012). Molecular diagnosis of infantile mitochondrial disease with targeted next-generation sequencing. Sci Transl Med 4, 118ra110.

62. Hamalainen RH, Manninen T, Koivumaki H, Kislin M, Otonkoski T, and Suomalainen A. (2013). Tissue- and cell-type-specific manifestations of heteroplasmic mtDNA 3243A>G mutation in human induced pluripotent stem cell-derived disease model. Proc Natl Acad Sci U S A 110, E3622–3630. [PubMed: 24003133]

63. Protasoni M, Pérez-Pérez R, Lobo-Jarne T, Harbour ME, Ding S, Peñas A, Diaz F, Moraes CT, Fearnley IM, Zeviani M, et al. (2020). Respiratory supercomplexes act as a platform for complex III-mediated maturation of human mitochondrial complexes I and IV. EMBO J 39, e102817.

64. Gerdes F, Tatsuta T, and Langer T. (2012). Mitochondrial AAA proteases--towards a molecular understanding of membrane-bound proteolytic machines. Biochim Biophys Acta 1823, 49–55. [PubMed: 22001671]

65. Wendler P, Ciniawsky S, Kock M, and Kube S. (2012). Structure and function of the AAA+ nucleotide binding pocket. Biochim Biophys Acta 1823, 2–14. [PubMed: 21839118]

66. Sallevelt SC, de Die-Smulders CE, Hendrickx AT, Hellebrekers DM, de Coo IF, Alston CL, Knowles C, Taylor RW, McFarland R, and Smeets HJ (2017). De novo mtDNA point mutations are common and have a low recurrence risk. J Med Genet 54, 73–83. [PubMed: 27450679]

67. Parsons JD (1995). Miropeats: graphical DNA sequence comparisons. Comput Appl Biosci 11, 615–619. [PubMed: 8808577]

68. Li H, and Durbin R. (2009). Fast and accurate short read alignment with Burrows-Wheeler transform. Bioinformatics 25, 1754–1760. [PubMed: 19451168]

69. Poplin R, Ruano-Rubio V, DePristo MA, Fennell TJ, Carneiro MO, Van der Auwera GA, Kling DE, Gauthier LD, Levy-Moonshine A, Roazen D, et al. (2017). Scaling accurate genetic variant discovery to tens of thousands of samples. bioRxiv 201178, 10.1101/201178.

70. Ivakhno S, Roller E, Colombo C, Tedder P, and Cox AJ (2018). Canvas SPW: calling de novo copy number variants in pedigrees. Bioinformatics 34, 516–518. [PubMed: 29028893]

71. Cingolani P, Platts A, Wang le L, Coon M, Nguyen T, Wang L, Land SJ, Lu X, and Ruden DM (2012). A program for annotating and predicting the effects of single nucleotide polymorphisms, SnpEff: SNPs in the genome of Drosophila melanogaster strain w1118; iso-2; iso-3. Fly (Austin) 6, 80–92. [PubMed: 22728672]

72. McLaren W, Gil L, Hunt SE, Riat HS, Ritchie GR, Thormann A, Flicek P, and Cunningham F. (2016). The Ensembl Variant Effect Predictor. Genome Biol 17, 122. [PubMed: 27268795]

73. Paila U, Chapman BA, Kirchner R, and Quinlan AR (2013). GEMINI: integrative exploration of genetic variation and genome annotations. PLoS Comput Biol 9, e1003153.

74. Gayevskiy V, Roscioli T, Dinger ME, and Cowley MJ (2019). Seave: a comprehensive web platform for storing and interrogating human genomic variation. Bioinformatics 35, 122–125. [PubMed: 30561546]

75. Puttick C, Kumar KR, Davis RL, Pinese M, Thomas DM, Dinger ME, Sue CM, and Cowley MJ (2019). mity: A highly sensitive mitochondrial variant analysis pipeline for whole genome sequencing data. bioRxiv 852210, 10.1101/852210.

76. Layer RM, Chiang C, Quinlan AR, and Hall IM (2014). LUMPY: a probabilistic framework for structural variant discovery. Genome Biol 15, R84.

77. Lake NJ, Webb BD, Stroud DA, Richman TR, Ruzzenente B, Compton AG, Mountford HS, Pulman J, Zangarelli C, Rio M, et al. (2017). Biallelic Mutations in MRPS34 Lead to Instability of the Small Mitoribosomal Subunit and Leigh Syndrome. Am J Hum Genet 101, 239–254. [PubMed: 28777931]

78. Lieber DS, Calvo SE, Shanahan K, Slate NG, Liu S, Hershman SG, Gold NB, Chapman BA, Thorburn DR, Berry GT, et al. (2013). Targeted exome sequencing of suspected mitochondrial disorders. Neurology 80, 1762–1770. [PubMed: 23596069]

79. Kohda M, Tokuzawa Y, Kishita Y, Nyuzuki H, Moriyama Y, Mizuno Y, Hirata T, Yatsuka Y, Yamashita-Sugahara Y, Nakachi Y, et al. (2016). A Comprehensive Genomic Analysis Reveals the Genetic Landscape of Mitochondrial Respiratory Chain Complex Deficiencies. PLoS Genet 12, e1005679.

80. Sadedin SP, Dashnow H, James PA, Bahlo M, Bauer DC, Lonie A, Lunke S, Macciocca I, Ross JP, Siemering KR, et al. (2015). Cpipe: a shared variant detection pipeline designed for diagnostic settings. Genome Med 7, 68. [PubMed: 26217397]

81. Akesson LS, Eggers S, Love CJ, Chong B, Krzesinski EI, Brown NJ, Tan TY, Richmond CM, Thorburn DR, Christodoulou J, et al. (2019). Early diagnosis of Pearson syndrome in neonatal intensive care following rapid mitochondrial genome sequencing in tandem with exome sequencing. Eur J Hum Genet 27, 1821–1826. [PubMed: 31358953]

82. Sadedin SP, Ellis JA, Masters SL, and Oshlack A. (2018). Ximmer: a system for improving accuracy and consistency of CNV calling from exome data. Gigascience 7.

83. Jiang Y, Oldridge DA, Diskin SJ, and Zhang NR (2015). CODEX: a normalization and copy number variation detection method for whole exome sequencing. Nucleic Acids Res 43, e39.

84. Zheng GX, Lau BT, Schnall-Levin M, Jarosz M, Bell JM, Hindson CM, Kyriazopoulou-Panagiotopoulou S, Masquelier DA, Merrill L, Terry JM, et al. (2016). Haplotyping germline and cancer genomes with high-throughput linked-read sequencing. Nat Biotechnol 34, 303–311. [PubMed: 26829319]

85. Li H. (2018). Minimap2: pairwise alignment for nucleotide sequences. Bioinformatics 34, 3094–3100. [PubMed: 29750242]

86. Hahne F, and Ivanek R. (2016). Visualizing Genomic Data Using Gviz and Bioconductor In Statistical Genomics. Methods in Molecular Biology vol 1418 Mathé E, and Davis S, eds. (New York, NY: Humana Press), pp. 335–351.

87. Livak KJ, and Schmittgen TD (2001). Analysis of relative gene expression data using real-time quantitative PCR and the 2(-Delta Delta C(T)) Method. Methods 25, 402–408. [PubMed: 11846609]

88. Madeira F, Park YM, Lee J, Buso N, Gur T, Madhusoodanan N, Basutkar P, Tivey ARN, Potter SC, Finn RD, et al. (2019). The EMBL-EBI search and sequence analysis tools APIs in 2019. Nucleic Acids Res 47, W636–W641. [PubMed: 30976793]

89. Frazier AE, and Thorburn DR (2012). Biochemical analyses of the electron transport chain complexes by spectrophotometry. Methods Mol Biol 837, 49–62. [PubMed: 22215540]

90. Pagnamenta AT, Taanman JW, Wilson CJ, Anderson NE, Marotta R, Duncan AJ, Bitner-Glindzicz M, Taylor RW, Laskowski A, Thorburn DR, et al. (2006). Dominant inheritance of premature

ovarian failure associated with mutant mitochondrial DNA polymerase gamma. Hum Reprod 21, 2467–2473. [PubMed: 16595552]

91. Smith PK, Krohn RI, Hermanson GT, Mallia AK, Gartner FH, Provenzano MD, Fujimoto EK, Goeke NM, Olson BJ, and Klenk DC (1985). Measurement of protein using bicinchoninic acid. Anal Biochem 150, 76–85. [PubMed: 3843705]
92. Johnston AJ, Hoogenraad J, Dougan DA, Truscott KN, Yano M, Mori M, Hoogenraad NJ, and Ryan MT (2002). Insertion and assembly of human tom7 into the preprotein translocase complex of the outer mitochondrial membrane. J Biol Chem 277, 42197–42204. [PubMed: 12198123]
93. Stroud DA, Formosa LE, Wijeyeratne XW, Nguyen TN, and Ryan MT (2013). Gene knockout using transcription activator-like effector nucleases (TALENs) reveals that human NDUFA9 protein is essential for stabilizing the junction between membrane and matrix arms of complex I. J Biol Chem 288, 1685–1690. [PubMed: 23223238]
94. Stroud DA, Surgenor EE, Formosa LE, Reljic B, Frazier AE, Dibley MG, Osellame LD, Stait T, Beilharz TH, Thorburn DR, et al. (2016). Accessory subunits are integral for assembly and function of human mitochondrial complex I. Nature 538, 123–126. [PubMed: 27626371]
95. Kulak NA, Pichler G, Paron I, Nagaraj N, and Mann M. (2014). Minimal, encapsulated proteomic-sample processing applied to copy-number estimation in eukaryotic cells. Nat Methods 11, 319–324. [PubMed: 24487582]
96. Tyanova S, Temu T, and Cox J. (2016). The MaxQuant computational platform for mass spectrometry-based shotgun proteomics. Nat Protoc 11, 2301–2319. [PubMed: 27809316]
97. Tyanova S, Temu T, Sinitcyn P, Carlson A, Hein MY, Geiger T, Mann M, and Cox J. (2016). The Perseus computational platform for comprehensive analysis of (prote)omics data. Nat Methods 13, 731–740. [PubMed: 27348712]

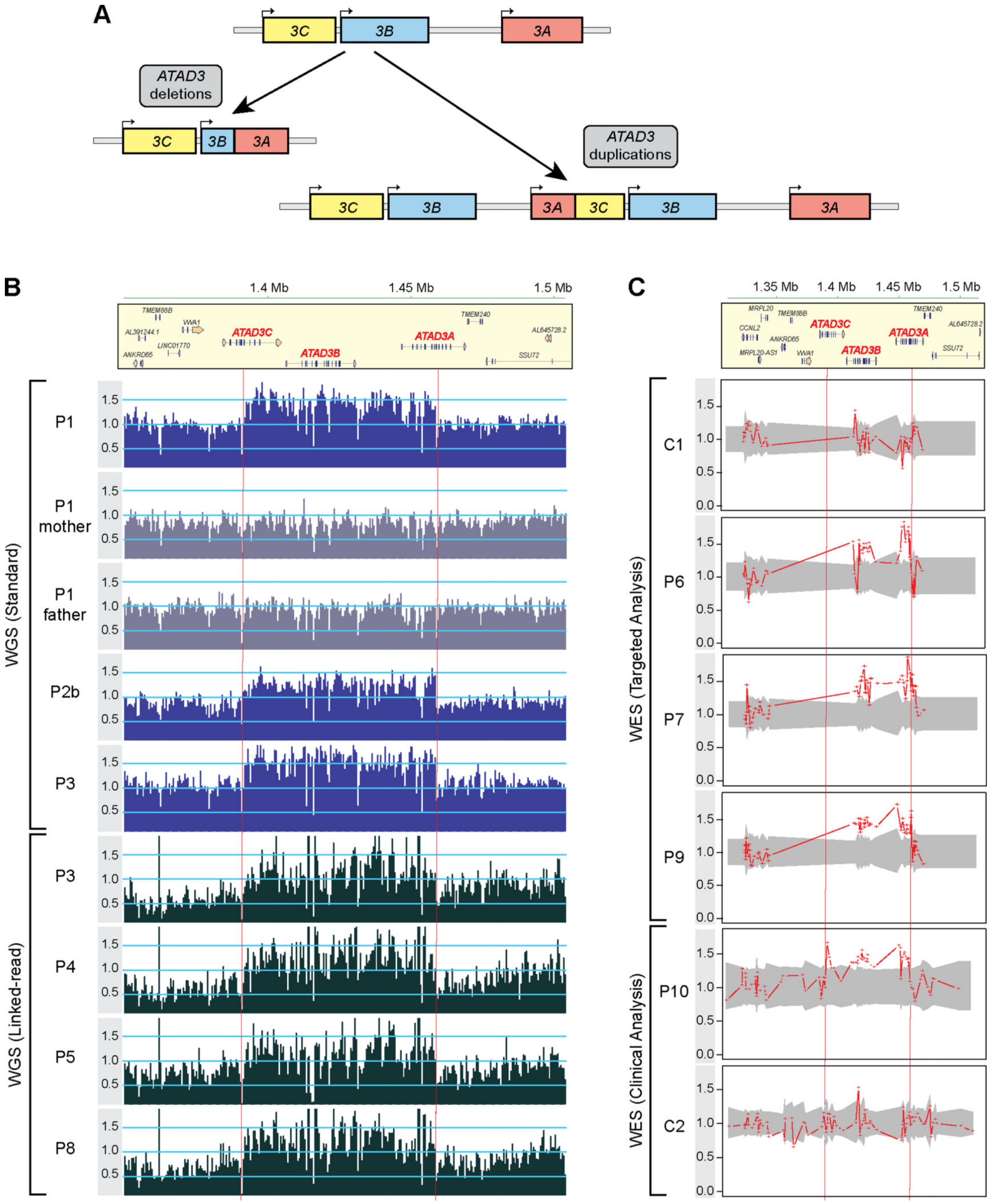

Figure 1. Detection of *ATAD3* duplications by genomic investigations.

A) The *ATAD3* locus is a site of genetic instability with recurrent pathogenic biallelic deletions and *de novo* duplications, resulting in chimeric *ATAD3B/ATAD3A* genes (deletions; expressed under the *ATAD3B* promoter) or *ATAD3A/ATAD3C* genes (duplications; expressed under the *ATAD3A* promoter). **B)** Read coverage across the chr1 region spanning the *ATAD3* locus and flanking genes as determined by either standard WGS in patients P1 and parents, P2b and P3 (upper panels with dark blue (patients) or grey (parents) bars) or 10x Genomics linked-read WGS in P3-P5 and P8 (lower panels with black bars). The number of uniquely mapping reads was determined for each 500 nt non-overlapping window. Read depths per bin were normalized by dividing by the median read count of all chr1 bins with non-zero read counts. Dashed red vertical lines indicate approximate breakpoints of the duplicated region. **C)** Samples were subjected to WES with either a targeted analysis of mitochondrial genes (control C1, patients P6, P7, and P9) or clinical analysis (control C2 and P10). ExomeDepth analysis across the *ATAD3* locus plotted as the ratio of the observed versus expected read depth. Shaded grey areas indicate 95% confidence interval across the matched reference set. See also Figure S1.

A

ID	Mutation	Breakpoint (*ATAD3A/ATAD3C*)	Duplication group	Identification
P1	NC_000001.10:g.1392270_1460317dup	intron11/intron7	*b*	WGS (Canvas SPW)
P2a/P2b	NC_000001.10:g.1391996_1460043dup	intron11/intron7	*b*	WGS (CNVnator)
P3	NC_000001.10:g.1392294_1460341dup	intron11/intron7	*b*	WGS (CNVnator)
P4	NC_000001.10:g.1391996_1460043dup	intron11/intron7	*b*	WES (ExomeDepth)
P5	NC_000001.10:g.1392560_1460670dup	exon12/exon8	c	WES (ExomeDepth)
P6	NC_000001.10:g.1391996_1460043dup	intron11/intron7	*b*	WES (ExomeDepth)
P7	NC_000001.10:g.1395419_1462718dup	intron13/intron9	*d*	WES (ExomeDepth)
P8	NC_000001.10:g.1391996_1460043dup	intron11/intron7	*b*	WES (ExomeDepth)
P9	NC_000001.10:g.1391996_1460043dup	intron11/intron7	*b*	WES (ExomeDepth)
P10	NC_000001.10:g.1391996_1460043dup	intron11/intron7	*b*	WES (XHMM)
P11	NC_000001.10:g.1391996_1460043dup	intron11/intron7	*b*	WES (XHMM)
P12	NC_000001.10:g.1391576_1459623dup	intron10/intron6	*a*	WES (XHMM)
P13	NC_000001.10:g.1391996_1460043dup	intron11/intron7	*b*	WES (XHMM)
P14	NC_000001.10:g.1391996_1460043dup	intron11/intron7	*b*	Clinical phenotype
P15	NC_000001.10:g.1391996_1460043dup	intron11/intron7	*b*	Microarray
P16	NC_000001.10:g.1391996_1460043dup	intron11/intron7	*b*	Clinical phenotype

B

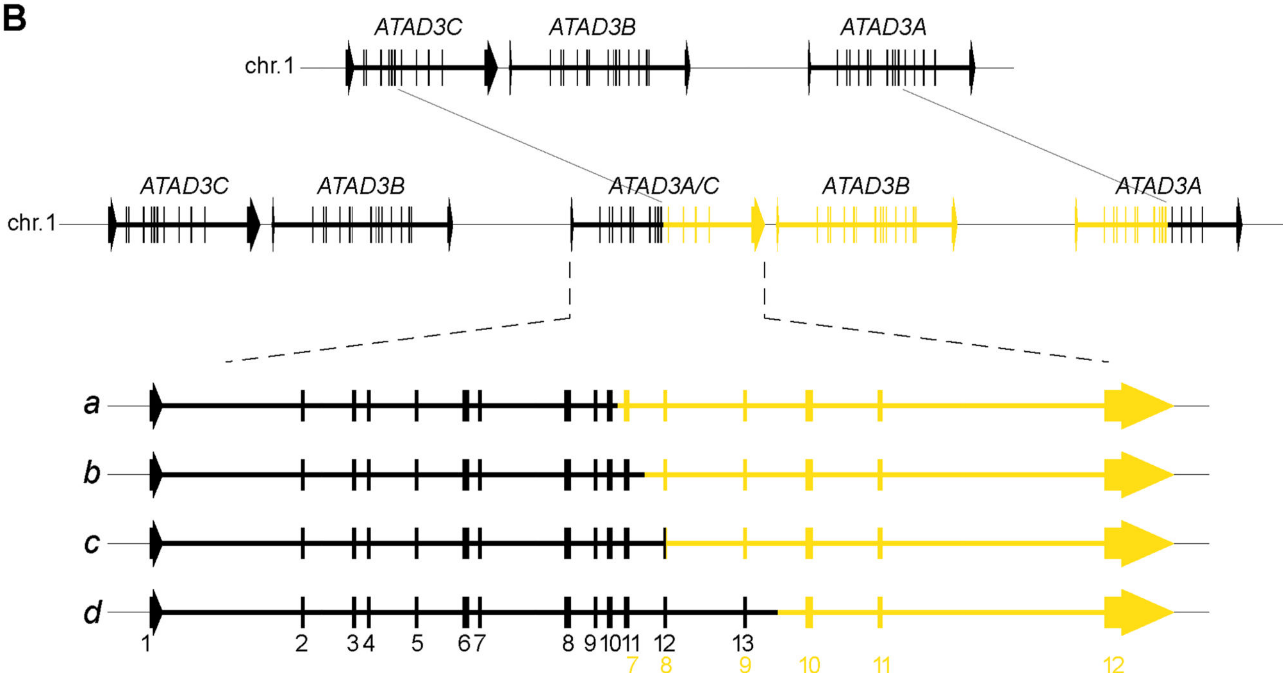

Figure 2. Analysis of *ATAD3* duplication breakpoints.

A) Sanger sequencing was used to determine genomic coordinates (GRCh37/hg19) for the *ATAD3* duplication in all patients, with the corresponding position of the breakpoint in the *ATAD3A* and *ATAD3C* genes indicated. The duplications were assigned to a group according to the location of the breakpoint within the genes. As well, the initial method and variant caller that led to the duplication identification is indicated. Duplications NC_000001.10:g.1392270_1460317dup and NC_000001.10:g.1391996_1460043dup have been previously reported[20]. **B)** Schematic of the most common *ATAD3* tandem duplication within the cohort (top, in yellow) validated by Sanger sequencing of gDNA breakpoints. The duplicated region (yellow) encompasses part of *ATAD3C*, all of *ATAD3B* and part of *ATAD3A*, resulting in a chimeric *ATAD3A*/*ATAD3C* gene. An expanded view of the chimeric *ATAD3A*/*ATAD3C* gene (bottom) indicates the different duplication groups (listed in **A**) and their impact on the gene structure. Corresponding exons are numbered at the bottom. black, *ATAD3A*; yellow, *ATAD3C*. See also Figure S2 and Table S2.

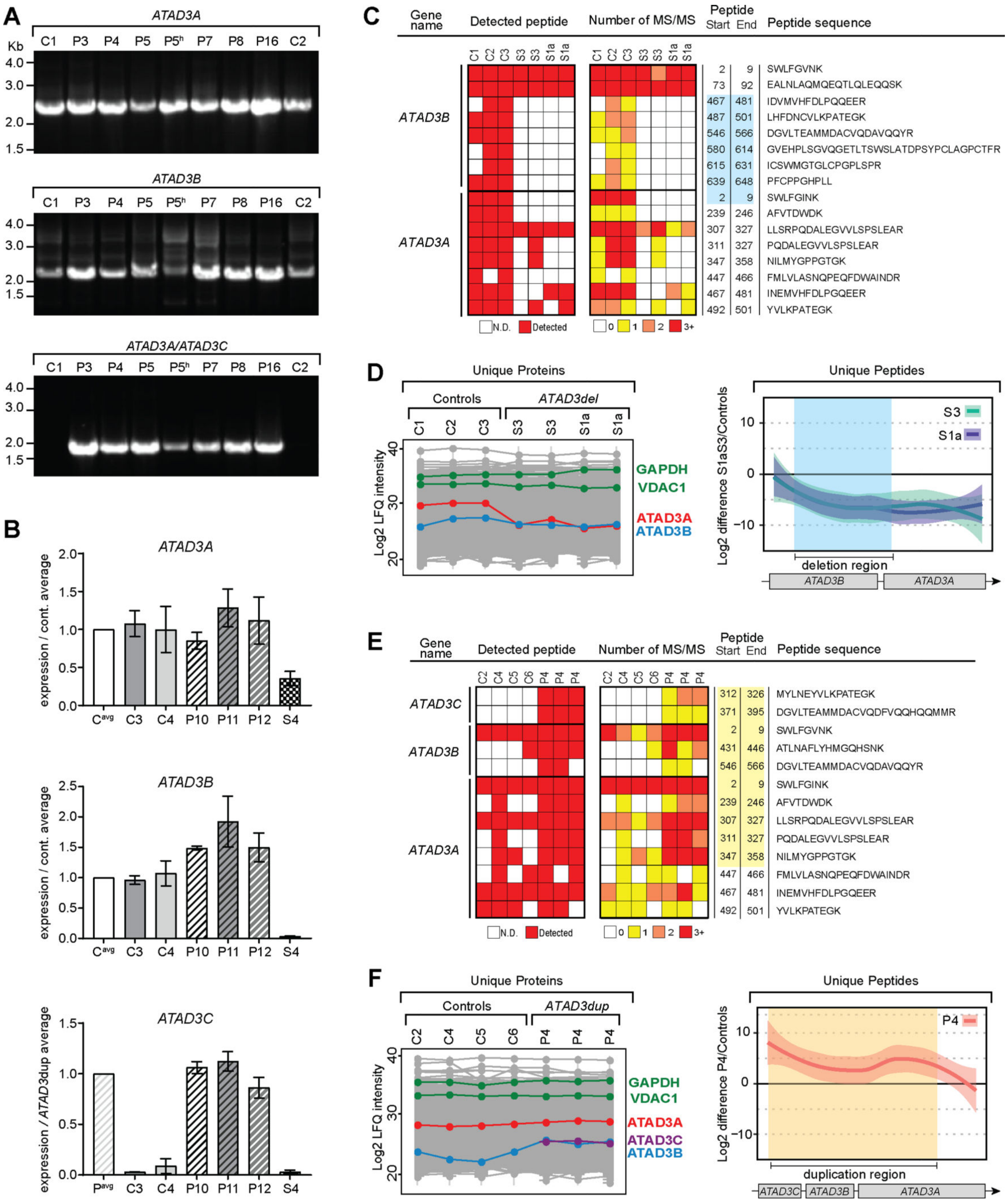

Figure 3. A chimeric *ATAD3A*/*ATAD3C* gene generated by the duplication is expressed.

A) cDNA generated from patient and control skin fibroblasts, and P5 heart (indicated by "h") was used for PCR amplification of transcripts from *ATAD3A*, *ATAD3B* and chimeric *ATAD3A*/*ATAD3C* genes. Transcripts were amplified using a primer targeting both *ATAD3A* and *ATAD3B*, and specific reverse primers for *ATAD3A*, *ATAD3B*, and *ATAD3C*. **B)** qRT-PCR was performed using cDNA from control and patient skin fibroblasts for quantitative analysis of transcripts using regions corresponding to *ATAD3A* and *ATAD3B* exons 15/16 and *ATAD3C* exons 11/12, which are the last exons of the genes. Values expressed relative to control average (*ATAD3A* and *ATAD3B*) or *ATAD3*dup patient average (*ATAD3C*). Shaded boxes, controls; dashed boxes, *ATAD3*dup patients; checked box, *ATAD3*del patient (S4). n = 3, error = SD. **C)** Label-free quantitative (LFQ) proteomics was performed on skin fibroblasts from controls (C; n=3) and *ATAD3*del patients[19] S3 and S1a (in duplicate). Unique ATAD3A and ATAD3B peptides were plotted according to their presence, as well as the number of MS/MS spectra observed. The blue box indicates the peptides encoded within the deleted *ATAD3* region. ATAD3C peptides were not detected in these samples. N.D., not detected. **D)** Using the LFQ proteomics data for all unique peptides from **C**, the relative levels of ATAD3A and ATAD3B proteins in each sample were compared (left panel), alongside the levels of cytosolic (GAPDH) and mitochondrial (VDAC1) marker proteins. The mean difference of Log_2 LFQ intensities between S3 and S1a to controls for individual peptides were plotted across the *ATAD3* locus with the deleted region indicated (blue shading) (right panel). Missing values for individual peptides were imputed as described in the methods and the loess smoothed curve plotted along with the 95% confidence interval (right panel). **E)** LFQ proteomics was performed on skin fibroblasts for controls (n=4) and *ATAD3*dup patient P4 (in triplicate), with unique peptides for ATAD3A, ATAD3B and ATAD3C plotted as in **C**. The yellow box indicates the peptides encoded within the duplicated *ATAD3* region. **F)** Using the LFQ proteomics data from **E**, the relative levels of ATAD3A, ATAD3B and ATAD3C proteins were compared across all samples (left panel). The mean difference of Log_2 LFQ intensities between P4 to controls were plotted across the ATAD3 locus as in **D**, with the duplication region indicated (yellow shading) (right panel). See also Figures S3 and S4.

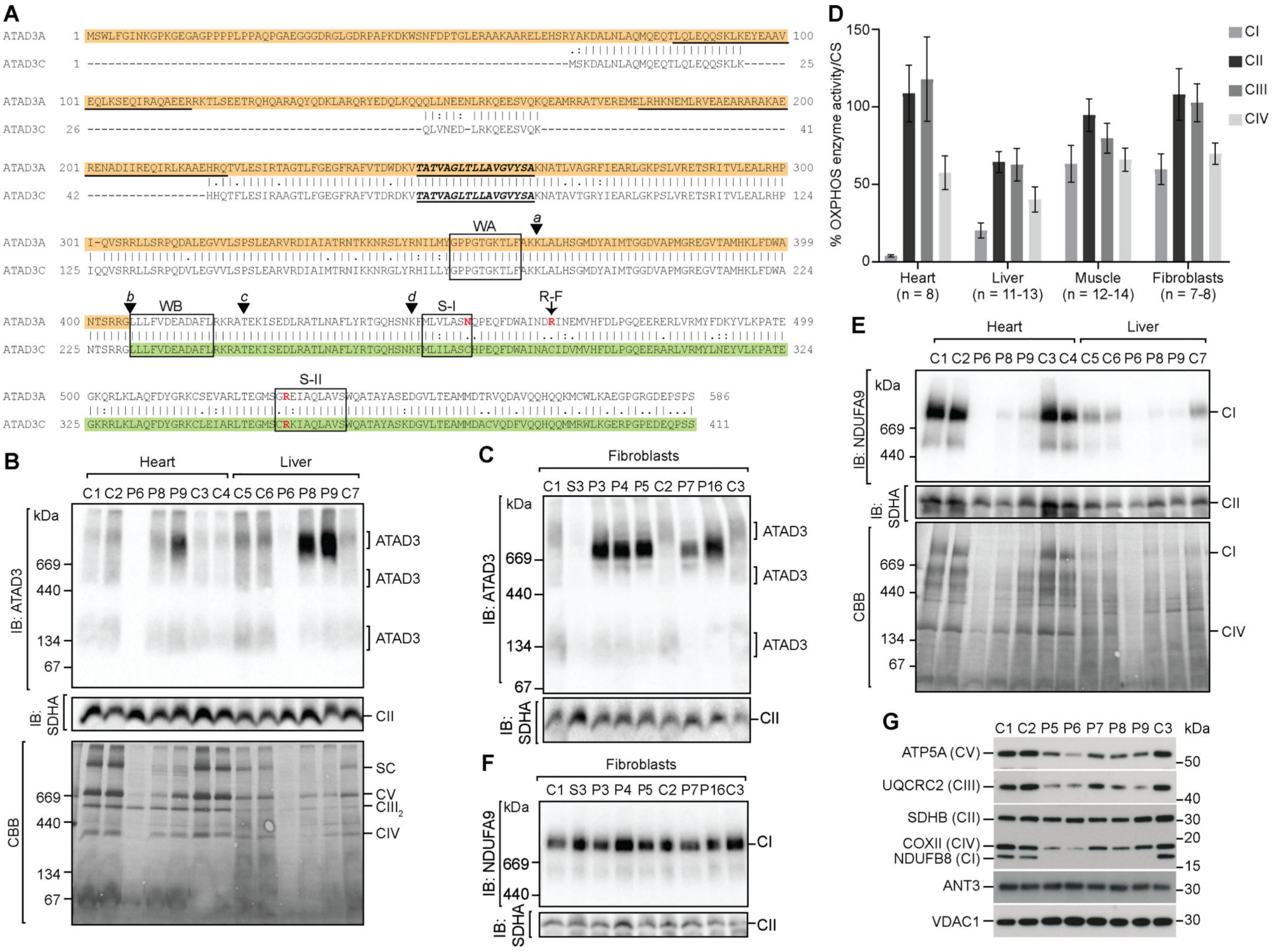

Figure 4. *ATAD3* duplication leads to OXPHOS complex I deficiency and ATAD3 oligomerization defects.

A) An alignment of ATAD3A (NP_001164006) with ATAD3C (NP_001034300) showing predicted protein domains and key residues[12,28,65]: coiled coil regions (underlined); transmembrane domain (underlined/ bold italic text); Walker A and Walker B motifs (WA and WB, boxed); Sensor I and Sensor II motifs (S-I and S-II, key residue in red); and arginine finger residue (R-F, red). The location of the breakpoints corresponding to the deletion groups (*a*-*d*) are indicated by arrowheads. The predicted chimeric ATAD3A/ ATAD3C protein generated by the most common duplication group group (*b*) corresponds to the ATAD3A region highlighted in orange, and the ATAD3C region highlighted in green. **B)** Mitochondria isolated from control and patient heart and liver biopsies were solubilized in 1% digitonin and subjected to blue native (BN)-PAGE and analysis of ATAD3 complexes by immunoblotting (anti-ATAD3), in comparison to OXPHOS complex II (anti-SDHA) (upper panels). Coomassie brilliant blue (CBB) staining of the membrane is shown to compare loading and sample integrity (lower panels). SC, supercomplex. **C)** Fibroblast mitochondria isolated from control, *ATAD3*dup patients and *ATAD3*del patient S3 cell lines analyzed by BN-PAGE as in **B**. **D)** OXPHOS enzyme activity normalized to citrate synthase (CS) activity and expressed as the percent of control mean was determined in patient tissue samples. Error

= SEM. **E)** Mitochondria isolated from control and patient heart and liver biopsies were solubilized in 1% Triton X-100 and subjected to BN-PAGE and analysis by immunoblotting for OXPHOS complex I (anti-NDUFA9) and complex II (anti-SDHA) (upper panels), with CBB staining shown for comparison. **F)** Fibroblast mitochondria isolated from control, *ATAD3*dup and *ATAD3*del patient S3 cell lines analyzed by BN-PAGE as in **E. G)** Total heart tissue lysates from controls and patients (2 µg) analyzed by SDS-PAGE and western blotting with antibodies against an antibody cocktail targeting individual OXPHOS complex subunits, and controls VDAC1 (porin) and ANT3. See also Figure S5 and Table S3.

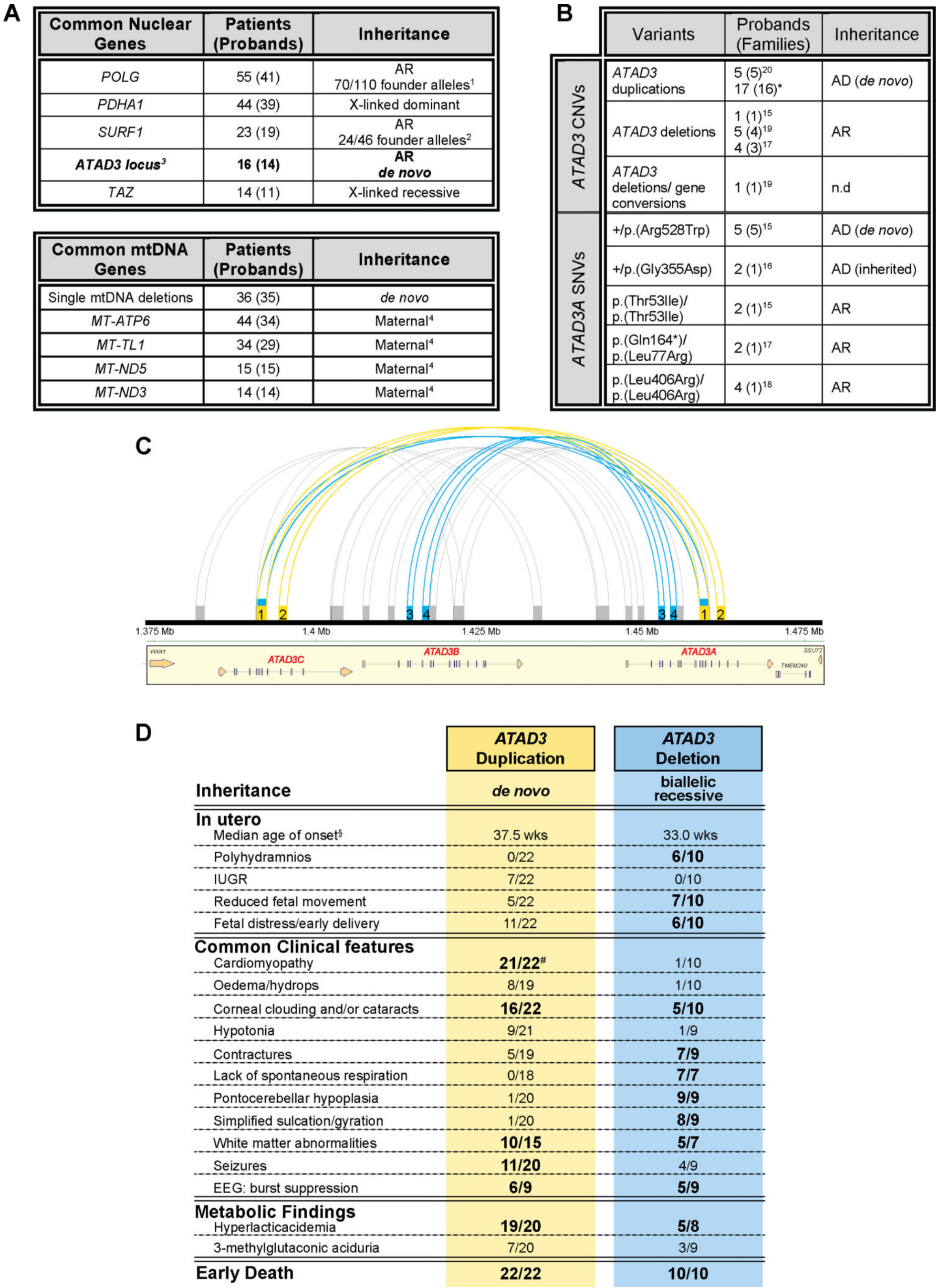

A

Common Nuclear Genes	Patients (Probands)	Inheritance
POLG	55 (41)	AR 70/110 founder alleles[1]
PDHA1	44 (39)	X-linked dominant
SURF1	23 (19)	AR 24/46 founder alleles[2]
ATAD3 locus[3]	**16 (14)**	**AR** ***de novo***
TAZ	14 (11)	X-linked recessive

Common mtDNA Genes	Patients (Probands)	Inheritance
Single mtDNA deletions	36 (35)	*de novo*
MT-ATP6	44 (34)	Maternal[4]
MT-TL1	34 (29)	Maternal[4]
MT-ND5	15 (15)	Maternal[4]
MT-ND3	14 (14)	Maternal[4]

B

	Variants	Probands (Families)	Inheritance
ATAD3 CNVs	*ATAD3* duplications	5 (5)[20] 17 (16)*	AD (*de novo*)
	ATAD3 deletions	1 (1)[15] 5 (4)[19] 4 (3)[17]	AR
	ATAD3 deletions/ gene conversions	1 (1)[19]	n.d
ATAD3A SNVs	+/p.(Arg528Trp)	5 (5)[15]	AD (*de novo*)
	+/p.(Gly355Asp)	2 (1)[16]	AD (inherited)
	p.(Thr53Ile)/ p.(Thr53Ile)	2 (1)[15]	AR
	p.(Gln164*)/ p.(Leu77Arg)	2 (1)[17]	AR
	p.(Leu406Arg)/ p.(Leu406Arg)	4 (1)[18]	AR

D

	ATAD3 Duplication	*ATAD3* Deletion
Inheritance	*de novo*	biallelic recessive
In utero		
Median age of onset§	37.5 wks	33.0 wks
Polyhydramnios	0/22	**6/10**
IUGR	7/22	0/10
Reduced fetal movement	5/22	**7/10**
Fetal distress/early delivery	11/22	**6/10**
Common Clinical features		
Cardiomyopathy	**21/22#**	1/10
Oedema/hydrops	8/19	1/10
Corneal clouding and/or cataracts	**16/22**	**5/10**
Hypotonia	9/21	1/9
Contractures	5/19	**7/9**
Lack of spontaneous respiration	0/18	**7/7**
Pontocerebellar hypoplasia	1/20	**9/9**
Simplified sulcation/gyration	1/20	**8/9**
White matter abnormalities	**10/15**	**5/7**
Seizures	**11/20**	4/9
EEG: burst suppression	**6/9**	**5/9**
Metabolic Findings		
Hyperlacticacidemia	**19/20**	**5/8**
3-methylglutaconic aciduria	7/20	3/9
Early Death	**22/22**	**10/10**

Figure 5. *ATAD3* regions prone to recurrent rearrangements causing overlapping clinical symptoms.

A) Summary of the five most common nuclear or mtDNA loci in which mutations cause pediatric mitochondrial disease, from our experience with molecular diagnosis of >500 pediatric-onset cases from Australia & New Zealand, including mutations in a total of 74 nuclear genes and 12 mtDNA genes plus mtDNA deletions. [a]*POLG* founder mutations of ancient European origin[47] comprise 40 p.(Ala467Thr) alleles, 15 p.(Trp748Ser) alleles and 15 p.(Gly848Ser) alleles; [b]*SURF1* c.311_312insATdel10 founder mutation appears to be of

European origin[48]; [c]*ATAD3* defects encompass pathogenic duplication and deletion rearrangements; [d]Up to a quarter of mtDNA mutations found in pediatric cases appear to be *de novo* mutations[66]. AR, autosomal recessive. **B)** Numerous pathogenic CNVs in the *ATAD3* locus and SNVs in *ATAD3A* have been identified. *ATAD3A* variants correspond to transcript NM_001170535. *, this study; AD, autosomal dominant; n.d., no data. **C)** Graphical illustration of tandem repeats in the *ATAD3* locus generated using Miropeats[67] with a similarity threshold of 900 bp. Regions of similarity associated with pathological *ATAD3* rearrangements are indicated for biallelic deletions (blue) and *de novo* duplications (yellow). All other regions of intragenic similarity in grey. *ATAD3* duplication groups *a-c* fall within region of similarity "1" and duplication group *d* within similarity region "2". *ATAD3C/ATAD3A* deletion breakpoints fall within similarity region "1" and *ATAD3B/ATAD3A* deletion breakpoints within regions "3" and "4". Region "1" spans across *ATAD3C* introns 4–7 and *ATAD3A* introns 8–11; region "2" across *ATAD3C* introns 8–9 and *ATAD3A* introns 12–13; region "3" across *ATAD3A* and *ATAD3B* introns 2–4; region "4" across *ATAD3A* and *ATAD3B* introns 4–5. **D)** Comparison of clinical features across all reported patients with *ATAD3* duplications and biallelic deletions[15,17,19,20] leading to severe presentations. Clinical features associated with more than 50% of *ATAD3*dup or *ATAD3*del patients in bold. §, median age of onset in weeks from conception; *ATAD3*dup patients n = 22 (average age of onset ± SD, 37.0 ± 3.4 weeks) or *ATAD3*del patients n = 10 (average age of onset ± SD, 32.7 ± 3.4). #, P4 with "borderline contractility" was not considered to have cardiomyopathy; 16/21 patients with cardiomyopathy were diagnosed with hypertrophic cardiomyopathy (HCM). EEG, electroencephalogram; MRI, magnetic resonance imaging.

Table 1.

Clinical Summary of *ATAD3* duplication patients[a].

Patient	Sex Ancestry	Age at Onset	Birth History	Age at Death	Cardiology	Ophthalmology	Brain imaging / neuropathology	Other Features	Biochemical investigations[b]
P1	F European (Dutch)	At birth 37/40	Caesarean 37/40	38 days	HCM	Bilateral cataract	MRI: diffuse hyperintense and swollen cerebral white matter on T2, hyperintense basal ganglia on T1, bilateral subependymal pseudocysts, mild pontocerebellar hypoplasia, lactate peak on MRS	Ascites, seizures, burst-suppression pattern (EEG)	Blood: lactate 1.7–2.9 mmol/L, abnormal liver function tests CSF: lactate 8.7 mmol/L Urine: increased TG, PG, IBG, IVG, 3MCG, alanine
P2a	M European (Australian)	At birth 37/40	Caesarean 37/40	6 days	HCM	Dense corneal clouding	Histopathology: widespread gliosis and microglial activation with some neuronal loss but no other apparent structural abnormalities	Hypotonia, seizures, burst-suppression pattern (EEG)	Blood: lactate > 3.5 mmol/L (persistent metabolic acidosis) Urine: slight increase in MMA, MC
P2b	M European (Australian)	At birth 37/40	Caesarean 37/40	5 days	HCM	Dense corneal clouding	Histopathology: microglial activation, gliosis with some neuronal loss and occasional necrotic neurons in the brainstem, cerebellar dentate nucleus, basal ganglia, thalamus, and subiculum. Cerebral white matter was relatively spared	Hypotonia, contractures, seizures	Blood: lactate > 3.5 mmol/L (persistent metabolic acidosis) Urine: slight increase in MMA, MC
P3	M European (Australian)	*In utero* 38/40	Caesarean 38/40	9 days	HCM	Bilateral corneal opacification	MRI: mild swelling and diffuse cerebral white matter hyperintensities on T2, bilateral cysts in the temporal lobes (particularly right side), lactate peak on MRS	IUGR, hypotonia, abnormal posturing, burst-suppression pattern (EEG)	Blood: lactate 3–7 mmol/L (persistent metabolic acidosis) CSF: lactate 15.8 mmol/L (1.5 hours postmortem) Urine: slight increase in 3MGA, lactate
P4	F European (Australian)	*In utero* 3rd trimester	Caesarean 39/40	4 days	Borderline contractility		MRI: increased cerebral white matter signal, high lactate peak and low NAA on MRS Cranial US: Echogenicity of the basal ganglia and left lenticular striate artery	IUGR, hip flexion contractures, seizures, hepatic hemosiderosis and steatosis	Blood: increasing lactates (persistent metabolic acidosis) 7mmol/L (at birth) to 21 mmol/L (50 hours >delivery)
P5	F Mauritian	*In utero* 36/40	Caesarean 36/40	3 days	HCM	Probable cataracts	Not performed	IUGR, hypotonia	Blood: lactate 9.1 mmol/L (persistent metabolic acidosis)
P6	M European (New Zealander)	*In utero* 38/40	Caesarean 38/40	3 days (64 hours)	HCM endocardial fibroelastosis	Corneal opacities, microphthalmia, possible cataracts	MRI: severely abnormal cerebral and cerebellar white matter signal and cerebral	Hydrops fetalis, seizures, burst-suppression pattern (EEG),	Blood: lactate peak 13 mmol/L (persistent metabolic acidosis) Urine: grossly elevated lactate and

Patient	Sex Ancestry	Age at Onset	Birth History	Age at Death	Cardiology	Ophthalmology	Brain imaging / neuropathology	Other Features	Biochemical investigations[b]
							swelling, subtle basal ganglia signal abnormality	hepatomegaly with macrovesicular steatosis	βOHB with TCA cycle intermediates including moderate increases in fumarate and 3MGA
P7	M European (Australian)	At birth 37/40	Caesarean 37/40	3 days	HCM endocardial fibrosis	Corneal opacities, periorbital conjunctival edema	Neuropathology: cerebral edema, poor demarcation between cortex and white matter, few areas of apparent softening in the subcortical white matter (right caudate nucleus and right fronto-parietal region)	IUGR, edema, seizures, brother died at 6 days following fetal distress/birth asphyxia	Blood: lactate 4 mmol/L, pyruvate 74 uMol/L, total carnitine 18 μM, free carnitine 12 μM CSF: lactate 4.5 mmol/L Urine: traces of fumaric, 3-methylglutaric and 3MGA
P8	M European (Australian)	*In utero* 38/40	Breech 38/40	8 days	HCM endocardial fibroelastosis		Cranial US: intraventricular hemorrhages, patchy hyperechogenicity in the basal ganglia consistent with calcium, right caudate cysts	Edema, hypotonia, hepatomegaly and steatosis	Blood: lactate peak 23.2 mmol/L, minimum pH 7.14
P9	F European (Australian)/ East Asian (Japanese)	*In utero* IUGR 26/40, reduced fetal movement 34/40	Caesarean 35/40	6 days	Dilated phase of HCM		Cranial US: sub-ependymal cysts and lenticular striate artery echogenicity	IUGR, oligohydramnios, hepatic hemosiderosis, renal failure	Blood: lactate 8.6–25 mmol/L (persistent metabolic acidosis) CSF: lactate 13.5 mmol/L
P10	M East Asian (Japanese)	At birth	40/40	2 months	HCM	Corneal clouding	MRI: cerebral white matter hyperintense lesions on T2	Hypotonia, neonatal asphyxia, bilateral hearing loss	Blood: lactate 9.9 mmol/L, pyruvate 0.36 mmol/L CSF: lactate 9.9 mmol/L, pyruvate 0.34 mmol/L
P11	M East Asian (Japanese)	At birth	37/40	1 month	HCM		Cranial US: bilateral bright thalami	Neonatal asphyxia, cardiac tamponade	Blood: lactate 12.3 mmol/L, pyruvate 0.46 mmol/L
P12	F East Asian (Japanese)	*In utero* 36/40	Caesarean 36/40	1 month	Heart failure, mild hypertrophy	Corneal clouding, microphthalmia, abnormal iris	Brain CT: mild calcification in lenticular nucleus	IUGR, arthrogryposis neonatal asphyxia	Blood: lactate 12.6 mmol/L, pyruvate 0.35 mmol/L
P13	F East Asian (Japanese)	At birth	40/40	10 days	HCM		Brain CT: diffuse cerebral white matter hypodensity and swelling plus low density in the basal ganglia and thalamus	Neonatal asphyxia	Blood: lactate12.3 mmol/L, pyruvate 0.25 mmol/L
P14	M European (Australian)	*In utero* 37/40	Induced 37/40	3 days	DCM	Bilateral corneal opacity, bilateral cataracts	Cranial US: bilateral subependymal hemorrhages Histopathology: widespread gliosis and microglial activation with some neuronal loss	Hydrops, seizures, burst-suppression pattern (EEG), congenital alveolar dysplasia, hepatic siderosis and microvesicular steatosis	Blood: lactate 2.3 – 15 mmol/L (persistent metabolic acidosis) Urine: grossly elevated lactate, slight fumarate and 3MGA

Patient	Sex Ancestry	Age at Onset	Birth History	Age at Death	Cardiology	Ophthalmology	Brain imaging / neuropathology	Other Features	Biochemical investigations[b]
P15	M European (Australian)	*In utero* 31/40		Fetal death *in utero* 36+6/40	HCM endocardial fibroelastosis		Histopathology: gliosis and microglial activation with some neuronal loss in the brainstem, cerebellum, thalamus and basal ganglia	IUGR, hydrops fetalis	No investigations performed (fetal death *in utero*)
P16	M European (Australian)	At birth	41.5/40	7 days	HCM	Corneal clouding	Brain MRI: mild signal abnormality and swelling of cerebral white matter, severe generalised encephalopathy, increased lactate on MRS	Seizures, renal failure	Blood: lactate 6.7 – 50 mmol/L (persistent metabolic acidosis) Urine: increased 3MGA, 3methylglutarate, fumarate and lactate

Abbreviations: ADC, apparent diffusion coefficient; β-OHB, β-hydroxybutyrate; CMV, cytomegalovirus; CSF, cerebral spinal fluid; CT, computed tomography; DCM, dilated cardiomyopathy; EEG, electroencephalogram; HCM, hypertrophic cardiomyopathy; IBC, isobutyrylglycine; IUGR, intrauterine growth restriction; IVG, isovalerylglycine; MC, methylcitrate; MMA, methylmalonic acid; MRI, magnetic resonance imaging; MRS, magnetic resonance spectroscopy; NAA, N-acetylaspartate; PG, propionylglycine; TG, tiglylglycine; US, ultrasound; 3MCG, 3-methylcrotonylglycine; 3MGA, 3-methylglutaconic acid.

[a] See also Table S1.

[b] Reference ranges for blood and CSF lactate and pyruvate levels varied between different centers and we regarded blood and CSF lactate levels as elevated if >2.2 mmol/L and blood and CSF pyruvate as elevated if >0.1 mmol/L.

KEY RESOURCES TABLE

REAGENT or RESOURCE	**SOURCE**	**IDENTIFIER**
Antibodies		
Rabbit anti-ATAD3	He et al., 2007	N/A
Rabbit anti-SLC25A6 (ANT3)	Abcam	Cat# ab154007; RRID: AB_2619664
Mouse anti-SDHA (complex II 70 kDa subunit)	Molecular Probes	Cat# A-11142; RRID: AB_221579
Mouse anti-SDHA (complex II 70 kDa subunit)	Abcam	Cat# ab14715; RRID: AB_301433
Mouse anti-VDAC1 (Porin)	Abcam	Cat# ab14734; RRID: AB_443084
Mouse Total OXPHOS Human WB Antibody Cocktail	Abcam	Cat# ab110411; RRID: AB_2756818
Rabbit anti-NDUFA9	Stroud et al., 2013	N/A
Rabbit anti-ATAD3A	Abnova	Cat# H00055210-D01; RRID: AB_10718149
Mouse anti-ATAD3B	Abnova	Cat# H00083858-B01P; RRID: AB_1571499
Mouse anti-TIM23	BD Bioscience	Cat# 611223; RRID: AB_398755
Mouse Anti-V5 tag	Invitrogen	Cat# R960-25; RRID: AB_2556564
Mouse anti-UQCRC1 (core 1) 16D10AD9AH5	Thermo Fisher Scientific	Cat# 459140; RRID: AB_2532227
Mouse anti-COX4	Abcam	Cat# ab110261; RRID: AB_10862101
Sheep anti-mouse IgG- horseradish peroxidase conjugated antibody	GE Healthcare	Cat# NA931; RRID: AB_772210
Donkey anti-rabbit IgG- horseradish peroxidase conjugated antibody	GE Healthcare	Cat# NA934; RRID: AB_772206
Bacterial and Virus Strains		
Biological Samples		
Human control and *ATAD3dup* patient tissue biopsies	This paper	N/A
Chemicals, Peptides, and Recombinant Proteins		
Triton X-100	Sigma Aldrich	Cat# T9284
Digitonin- High purity	Merck	Cat# 300410
Lipofectamine2000	ThermoFisher Scientific	Cat# 11668030
RIPA buffer	Nacalai Tesque	Cat# 16488-34
Protein G-Sepharose	Sigma	Cat# P3296
MS grade trypsin	Thermo Scientific	Cat# LTS90057
Critical Commercial Assays		
Clarity Western ECL Substrate	Bio-Rad	Cat# 170-5060
SureSelect Human all exome V5	Agilent Technologies	Cat# 5190-6209
TruSeq exome enrichment kit	Agilent Technologies	Cat# FC-121-1008
SureSelect QXT Reagent Kit CRE V1	Agilent Technologies	Cat# G9681B
SureSelect XT CRE V2	Agilent Technologies	Cat# 5190-9493
Nucleobond CB20	Macherey-Nagel	Cat# 740507
Qubit (dsDNA High Sensitivity kit)	Thermo Fisher Scientific	Cat# Q32851
TapeStation genomic DNA ScreenTape	Agilent Technologies	Cat# 5067-5365

REAGENT or RESOURCE	**SOURCE**	**IDENTIFIER**
TapeStation genomic DNA Reagents	Agilent Technologies	Cat# 5067-5366
Chromium™ Genome Chip Kit v2	10x Genomics	Cat# 120257
TapeStation High Sensitivity D1000 ScreenTape	Agilent Technologies	Cat# 5067-5584
TapeStation High Sensitivity D1000 Reagents	Agilent Technologies	Cat# 5067-5585
1D ligation library prep kit	Oxford Nanopore Technologies	Cat# SQK-LSK109
PromethION flow cell	Oxford Nanopore Technologies	Cat# FLO-PRO002
Infinium Global Screening Array-24 (GSA) v3.0 kit	Illumina	Cat# 20030770
Expand long range dNTPack kit	Roche	Cat# 04 829 034 001
TRIzol RNA isolation reagent	Invitrogen	Cat# 15596018
SuperScript IV First-Strand Synthesis System	Invitrogen	Cat#18091200
Power SYBR Green PCR Master Mix	Applied Biosystems	Cat# 4368577
Lipofectamine2000	ThermoFisher Scientific	Cat# 11668030
Deposited Data		
Experimental Models: Cell Lines		
Human control and *ATAD3dup* patient skin fibroblast cell lines	This paper	N/A
HEK293FT	ThermoFisher Scientific	Cat# R70007
Experimental Models: Organisms/Strains		
Oligonucleotides		
See Supplemental Table 2 for complete list of primers	This paper	N/A
Recombinant DNA		
CS-CA-MCS plasmid	Riken BRC DNA Bank	Cat# RDB05963
Software and Algorithms		
BWA-mem	Li and Durbin, 2009	http://bio-bwa.sourceforge.net/; RRID: SCR_010910
GATK HaplotypeCaller	Poplin et al., 2017	https://gatk.broadinstitute.org/hc/en-us; RRID: SCR_001876
canvas SPW	Ivakhno et al., 2018	https://github.com/Illumina/canvas
SnpEff	Cingolani et al., 2012	http://snpeff.sourceforge.net/; RRID: SCR_005191
ENSEMBL's VEP	McLaren et al., 2016	http://www.ensembl.org/info/docs/tools/vep/index.html; RRID: SCR_007931
Gemini	Paila et al., 2013	https://gemini.readthedocs.io/en/latest/; RRID: SCR_014819
Seave	Gayevskiy et al., 2019	https://github.com/KCCG/seave
Mity	Puttick et al., 2019	https://github.com/KCCG/mity
ClinSV	Minoche et al, *manuscript in preparation*	https://github.com/KCCG/ClinSV
ExomeDepth	Plagnol et al., 2012	https://cran.r-project.org/web/packages/ExomeDepth/; RRID: SCR_002663
XHMM	Fromer et al., 2012	https://statgen.bitbucket.io/xhmm/
Cpipe	Sadedin et al., 2015	https://melbournegenomics.github.io/

REAGENT or RESOURCE	SOURCE	IDENTIFIER
Ximmer	Sadedin et al., 2018	http://ssadedin.github.io/ximmer/; RRID: SCR_016427
bcl2fastq2	Ilumina	https://sapac.support.illumina.com/sequencing/sequencing_software/bcl2fastq-conversion-software.html; RRID:SCR_015058
LongRanger	10x Genomics	https://support.10xgenomics.com/genome-exome/software/pipelines/latest/installation
MinKNOW	Oxford Nanopore Technologies	https://nanoporetech.com/community
Guppy	Oxford Nanopore Technologies	https://nanoporetech.com/community
minimap2	Li, 2018	https://lh3.github.io/minimap2/
R	N/A	https://www.r-project.org/; RRID: SCR_001905
RStudio	RStudio	https://rstudio.com/; RRID: SCR_000432
ggplot2	N/A	https://cran.r-project.org/web/packages/ggplot2/index.html; RRID: SCR_014601
Bioconductor Gviz package	Hahne and Ivanek, 2016	https://bioconductor.org/packages/release/bioc/html/Gviz.html
KaryoStudio	Illumina	https://sapac.support.illumina.com/array/array_software/karyostudio.html
Miropeats	Parsons, 1995	http://www.littlest.co.uk/software/bioinf/old_packages/miropeats/
MaxQuant platform	Tyanova, Temu and Cox, 2016	https://www.maxquant.org/; RRID: SCR_014485
Perseus platform	Tyanova, Temu, Sinitcyn, et al., 2016	https://www.maxquant.org/perseus/; RRID: SCR_015753
Other		
Empore™ SDB-RPS (styrenedivinylbenzene-reverse phase sulfonate) solid phase extraction disk	Supelco Analytical	Cat# 66886-U
Empore™ Cation Exchange-SR solid phase extraction disk	Supelco Analytical	Cat# 66889-U
Empore™ SDB-XC poly(styrene-divinyl-benzene) solid phase extraction disk	Supelco Analytical	Cat# 66884-U
Pierce C18 Spin Tips	Thermo Scientific	Cat# LTS84850